THE ASTROPHYSICAL JOURNAL, 485:1–21, 1997 August 10

MEASUREMENTS OF THE SUNYAEV-ZELDOVICH EFFECT IN THE NEARBY CLUSTERS A478, A2142, AND A2256

S. T. MYERS,[1] J. E. BAKER,[2] A. C. S. READHEAD, AND E. M. LEITCH
Owens Valley Radio Observatory, 105-24 Caltech, Pasadena CA 91125

AND

T. HERBIG
Princeton University, Physics Department, Jadwin Hall, P.O. Box 708, Princeton, NJ 08544

Received 1996 May 15; accepted 1997 March 13

ABSTRACT

An X-ray flux-limited sample of nearby clusters of galaxies has been defined for observations of the Sunyaev-Zeldovich effect (SZE) to be carried out on the Owens Valley 5.5 m telescope at 32 GHz. The X-ray sample selection minimizes the systematic errors introduced by cluster elongation in the determination of H_0. Owing to their proximity, these clusters are well studied in the X-ray wave bands. The measurement of the SZE in three of these clusters is reported in this paper: $\Delta T = -375 \pm 28$ μK (A478), -437 ± 25 μK (A2142), and -243 ± 29 μK (A2256). These values have been corrected for radio source contamination, but have not been corrected for the beam dilution and switching (which are model dependent). There is an additional overall calibration uncertainty of 7%. If the temperature profile of the clusters is known, then the SZE provides a direct probe of the baryonic mass in the hot ionized phase of the medium. We find surface baryonic mass densities of $(7.5 \pm 2.5) \times 10^{13}\ M_\odot\ \mathrm{Mpc}^{-2}$ within the 7.′35 FWHM Gaussian beam of the 5.5 m telescope projected on the cluster centers. For A2142, A2256, and the Coma cluster previously observed by Herbig et al., we find a consistent value for the ratio of the SZE determined baryonic mass to the gravitational binding mass of $M_{\mathrm{sze}}/M_{\mathrm{tot}} = 0.061 \pm 0.011\ h^{-1}$. Note that this is a *lower limit* on the total baryon fraction, as there may be significant contributions from other baryons. Comparison with the standard big bang nucleosynthesis prediction $\Omega_B h^2 = 0.013 \pm 0.02$ gives a value for the cosmological density parameter of $\Omega_0 h \lesssim 0.21 \pm 0.05$, assuming our limit on the baryon fraction in clusters applies to the universe as a whole. This density is in agreement with independently determined values from large-scale structure studies. Recent values for $\Omega_B h^2$ based upon deuterium abundances are outside the previously accepted range, and in combination with our data lead to significantly higher or lower Ω_0. Finally, we present preliminary determinations of the Hubble constant using X-ray models gleaned from the literature. The data from the three clusters, along with the results previously obtained using the same telescope on the Coma Cluster, yield a sample average value $H_0 = 54 \pm 14$ km s^{-1} Mpc^{-1}. We discuss the uncertainties in these results and future prospects for this method.

Subject headings: cosmic microwave background — cosmology: observations — dark matter — distance scale — galaxies: clusters: general — intergalactic medium

1. INTRODUCTION

The scattering of the cosmic microwave background radiation by hot gas in clusters of galaxies, known as the Sunyaev-Zeldovich effect (SZE), has been recognized for over two decades as a potentially important tool for cosmological and astrophysical studies (Sunyaev & Zeldovich 1980). In the SZE, inverse Compton scattering boosts the microwave background photons to higher frequencies, upshifting and distorting the Planck blackbody spectrum. At low frequencies where the spectrum rises with frequency, this reduces the intensity of the CMB at a given frequency. At higher frequencies where the spectrum falls with frequency, the SZE increases the intensity. Relative to the background, clusters look dark at low frequencies and bright at high frequencies.

A particularly important application of SZE observations is the determination of the Hubble constant, H_0. Classical determinations of H_0 rely upon the cosmic distance ladder (see, e.g., Tully 1988) and are therefore subject to the uncertainties inherent in each step of the ladder. For this reason "direct" determinations of H_0 would be very important if the systematic errors could be understood and allowed for. Examples of such direct methods are expanding supernova photospheres, gravitational lenses, and the SZE. For recent determinations of H_0 using classical methods, see Kennicutt, Freedman, & Mould (1995) and references therein, as well as Sandage (1996) and Mould et al. (1995).

The high-temperature ionized cluster medium produces both Compton scattering (SZE) and thermal bremsstrahlung (X-ray) emission that depend upon different powers of the electron density and temperature, $n_e T_e$ for the SZE, and approximately $n_e^2 T_e^{1/2}$ for the bremsstrahlung component of the X-ray. The integral equations for the observed SZE and X-ray brightness can, given a suitable model for the density profile and knowledge of the electron gas temperature, be solved for central density and the linear core radius—when combined with the observed angular core radius, this yields a value for the angular diameter distance D_a. For clusters at low redshift, this yields the Hubble constant H_0. For a set of clusters covering a wide range of redshifts, the determination of $D_a(z)$ as a function of redshift

[1] Present address: Department of Physics and Astronomy, David Rittenhouse Laboratory, University of Pennsylvania, 209 South 33rd Street, Philadelphia, PA 19104-6396.

[2] Present address: Department of Astronomy, Campbell Hall, University of California, Berkeley, CA 94720.

z can constrain or determine other cosmological parameters such as the density parameter Ω_0 and cosmological constant Λ_0.

The gas in a massive galaxy cluster has a temperature of roughly 10^8 K and a central density in excess of 10^{-3} cm^{-3}. This leads to an expected microwave decrement along the line of sight through the cluster center in the range 0.1–1 mK. Despite the large size of the SZE relative to intrinsic anisotropy signals ($\lesssim 50$ μK), observations of the effect have proven difficult and have been plagued by systematic errors. However, a number of experiments have now produced reliable SZE measurements. Using the 40 m telescope at Owens Valley Radio Observatory (OVRO) at 20 GHz, Birkinshaw (1990) found ΔT_{RJ} of -444 ± 65 μK, -301 ± 49 μK, and -354 ± 43 μK for the clusters 0016+16, Abell 665, and Abell 2218, respectively. Herbig et al. (1995) measured a decrement of -308 ± 51 μK in the Coma Cluster using the OVRO 5.5 m telescope. Recent interferometric measurements of the SZE in A2218 (Jones et al. 1993) and A773 (Grainge et al. 1994) using the Ryle telescope at 15 GHz have been reported. Interferometric measurements of 0016+16 and A773 have also been made by Carlstrom, Joy, & Grego (1996) with the OVRO Millimeter Array outfitted with 32 GHz receivers. The SZE in the cluster A2163 has been measured using a bolometer array on the CSO (Wilbanks et al. 1994)—this measurement of the effect as an increment on the high-frequency side of the blackbody peak is the first to place interesting limits on the peculiar motion of massive clusters.

These observations have all been made on fairly distant clusters. This has been dictated by the use of large single dishes or large interferometers. These instruments have small switching angles or small fields of view that resolve out the structure on the angular scales corresponding to nearby clusters. In the determination of H_0, the models of the X-ray–emitting gas in the cluster potential are just as important as the SZE measurements. Accurate models are available only for the nearby clusters. Also, the control of biases to the H_0 determination, such as cluster elongation or substructure, requires the systematic study of a complete sample of carefully selected clusters. At the present, the best samples for this study are drawn from nearby ($z < 0.1$) X-ray–selected cluster catalogs.

The newly completed 5.5 m telescope at OVRO is an ideal instrument for SZE measurements in a sample of nearby clusters. The telescope operates at 32 GHz and has a sensitive wide-bandwidth HEMT receiver. The primary beam is 7.′35 (FWHM), and the dual-horn switching angle is 22.′16. This telescope has the right beam width and sensitivity to measure the SZE in clusters with angular core radii in the range 1′–22′ with reasonable efficiency. The Herbig et al. (1995) measurements of the Coma Cluster ($z = 0.023$) recovered approximately 61% of the central decrement.

We report here the first SZE observations undertaken with the specific aim of estimating and, where possible, eliminating the major known sources of systematic error in the determination of H_0 by means of SZE observations of a sample of nearby clusters.

2. THE X-RAY CLUSTER SAMPLE

There are three potential problems in SZE determinations of H_0: elongation, density substructure, and nonisothermality of the cluster gas. If a cluster is elongated along the line of sight, then H_0 will be underestimated, while if the cluster is elongated in the plane of the sky, then H_0 will be overestimated. Clumping of the intracluster medium also causes a bias, owing to the different dependences of the X-ray emission and SZE upon the electron density and temperature. In this case, H_0 is overestimated by the factor $\langle n_e^2 \rangle / \langle n_e \rangle^2$, a quantity that is always greater than unity. The measurement of H_0 is proportional to $T_e^{3/2}$, so errors in temperature or temperature gradients will be a problem. Detailed discussion of these problems have been presented in the literature (see, e.g., Birkinshaw, Hughes, & Arnaud 1991).

The uncertainties due to substructure and isothermality can be resolved only through high-resolution X-ray observations and detailed modeling. For this to be possible, nearby clusters must be chosen—new measurements by *ASCA* and *ROSAT* of these objects are revolutionizing our understanding of cluster astrophysics. However, if clusters are prolate or oblate ellipsoids, axial ratios of 0.5 imply an uncertainty of up to a factor of 2 in the line-of-sight distance through the cluster. This uncertainty will average out in determinations of H_0 if the SZE is measured in a large enough orientation unbiased sample of clusters. A sample chosen by central X-ray surface brightness will be systematically biased toward clusters that have long axes along the line of sight. Such a bias arises because these clusters will have a greater central brightness than clusters at the same distance with their short axes along the line of sight. To guard against this selection effect, it is necessary to choose a complete flux-limited parent sample while staying sufficiently above the sample flux limit to minimize the biasing effect upon the selection.

We selected the X-ray flux-limited sample of Edge et al. (1990) for our parent sample. This sample is complete for fluxes in the 2–10 keV band $f_X \geq 3.1 \times 10^{-11}$ ergs cm^{-2} s^{-1} and is 70%–90% complete at $f_X \geq 1.7 \times 10^{-11}$ ergs cm^{-2} s^{-1}. This sample was derived by Edge et al. from *HEAO-1* and *Ariel V* surveys and cross-checked with *Einstein* and *EXOSAT* observations.

We restrict our observations to the higher flux limit $f_X \geq 3.1 \times 10^{-11}$ ergs cm^{-2} s^{-1}, Galactic latitude $|b| \geq 20°$, and $\delta \geq -23°$. A high-luminosity subsample was selected with $L_X \geq 1.25 \times 10^{44}\ h^{-2}$ ergs s^{-1} (2–10 keV), where $H_0 = 100\ h$ km s^{-1} Mpc^{-1}. The 11 clusters in this subsample are listed in Table 1. The core radii for these clusters fall within the optimum size range for the 5.5 m telescope. Also, given the X-ray parameters for these clusters, we expect SZE decrements in the range 250–750 μK, which are easily observable with our system sensitivity. The redshifts and thus the luminosities listed in Table 1 were taken from the Edge et al. (1990) paper.

The Edge et al. sample for $f_X \geq 3.1 \times 10^{-11}$ ergs cm^{-2} s^{-1} is complete for $z \leq 0.066$ at $L_X \geq 1.5 \times 10^{44}\ h^{-2}$ ergs s^{-1}. The lowest luminosity cluster in our sample is Coma ($L_X = 1.85 \times 10^{44}\ h^{-2}$ ergs s^{-1})—at this luminosity, the sample would be complete for $z \leq 0.073$. The most distant cluster in our sample is A2142 ($z = 0.09$); at this redshift, the sample would be complete for $L_X \geq 2.82 \times 10^{44}\ h^{-2}$ ergs s^{-1}. In order to be able to observe a reasonably large number of clusters, we choose to use the entire sample, though it is flux limited only, and not volume limited out to $z = 0.1$. This means, therefore, that we are prone at the lowest luminosity levels to selection effects such as elongation, and some care will have to be taken in the interpretation of the statistical results.

TABLE 1

THE X-RAY–SELECTED SAMPLE

CLUSTER	POSITION (B1950)[a] R.A.	Decl.	z[b]	f_X (10^{-11} ergs cm^{-2} s^{-1})[b]	L_X (10^{44} h^{-2} ergs s^{-1})[b]	kT[c] (keV)	θ_{core}[d] (arcmin)
A85	00:39:19.5	−09:34:23	0.0518	6.37	1.88	6.2	2.51
A399	02:55:07.6	+12:50:47	0.0715	3.41	1.94	5.8	1.91
A401	02:56:12.0	+13:22:43	0.0748	5.88	3.68	7.8	4.68
A478	04:10:40.1	+10:20:21	0.0900	6.63	6.02	6.6	1.85
A754	09:06:49.7	−09:28:57	0.0528	8.53	2.62	9.1	8.45
A1651.....	12:56:48	−03:55:00	0.0825	3.67	2.80	7.0	...
Coma	12:57:19	+28:13:24	0.0232	25.4	1.49	8.1	10.5
A1795.....	13:46:35.4	+26:50:23	0.0616	5.30	2.23	5.3	3.03
A2029.....	15:08:27.2	+05:55:56	0.0767	7.52	4.92	7.8	1.58
A2142.....	15:56:15.8	+27:22:38	0.0899	7.50	6.80	8.7	3.69
A2256.....	17:06:56.3	+78:43:02	0.0601	5.20	2.08	7.5	5.33

NOTE.—Units of right ascension are hours, minutes, and seconds, and units of declination are degrees, arcminutes, and arcseconds.

[a] Positions from *Einstein* IPC, except A1651 from Abell et al. 1989.

[b] Redshifts, X-ray fluxes, and luminosities (2–10 keV) from Edge et al. 1990. Luminosities assume $q_0 = 1/2$.

[c] X-ray temperatures from *Einstein* MPC (David et al. 1993) except A478 from *Ginga* and *ROSAT* (Allen et al. 1993); A1651 from *HEAO-1* (Edge et al. 1990); Coma, A1795, A2142, A2256 from *Ginga* (David et al. 1993).

[d] Core radii from Jones & Forman 1984 except A401, A754, A2142 from Abramopoulos & Ku 1983; A478 from Allen et al. 1993; Coma from Briel et al. 1992; A2256 from Henry et al. 1993.

From the parent sample, we have selected for our first observations clusters that are free of strong radio sources that would contaminate our SZE measurements at 32 GHz. The clusters A478 and A2142, massive clusters with well-measured X-ray profiles, were ideal targets, with large expected SZE decrements. The cluster A2256 is optimal because of its high declination. The Coma Cluster was previously observed with this instrument by Herbig et al. (1995) and has been included in the sample.

3. OBSERVATIONS

Although SZE signals are roughly an order of magnitude larger than the limits that have been placed on intrinsic anisotropy signals, the removal of systematic effects from SZE data still requires great care. The SZE measurements must be very sensitive, with uncertainties less than 10% in order to contribute less than 20% to the uncertainty in the estimate of H_0. Most clusters are tracked over large angular distances across the sky. The variation of azimuth and zenith angle can introduce significant ground spillover effects, which can be minimized in intrinsic anisotropy observations by observing only fields near the north celestial pole. Our observations of clusters use a three-level differencing technique to remove systematic effects from ground spillover, the atmosphere, and the receiver.

The observations reported here were made between 1993 July 15 and 1994 March 6. The 5.5 m telescope at OVRO was used, employing a receiver operating at a center frequency of 32 GHz, with a primary beam FWHM of 7.′35. The receiver noise level for a measurement was approximately 0.9 mK in 1 s of total integration time. The noise level including atmosphere and ground pickup is about 50% higher than this. The receiver is discussed in § 3.1. and the sensitivity and noise performance in § 3.4.

This section contains detailed descriptions of the observing, calibration, data editing, filtering, and analysis procedures. Much of the discussion in may be skipped by the casual reader, though it is suggested that the reader look at the discussion of the referencing in § 3.2 and the data analysis in § 3.5 before proceeding to the presentation of the results for the cluster observations in § 4.

3.1. *First and Second Differencing*

The receiver has two horns: ANT (antenna) and REF (reference). These have nearly identical Gaussian on-sky response patterns with 7.′35 FWHM and a separation of 22.′16. The rms pointing accuracy of the 5.5 m telescope was found to be better than 0.′5 from observations of bright calibration sources. The receiver switches between the two beams every 1 ms ($f = 500$ Hz) by means of a pulse-latched switch. The output of the switch then passes through an amplifier chain before detection. Our observations employed as the first stage a TRW InSb HEMT amplifier with a bandwidth of 5.7 GHz centered at 32 GHz. After detection, the power measurements taken in each switch orientation are accumulated, and the mean difference and the standard deviation of the mean difference are computed for each 1 s fundamental integration period. This first level of switching removes the offsets and signal common to both beams and cancels the offsets due to low-frequency gain fluctuations in the amplifier chain.

Another level of switching is required to remove gradients. The telescope is moved in azimuth by the switching angle 22.′16, and a second difference is formed. The period for this switching is 20–50 s. The second differencing removes gradients in the atmospheric emission that are stable on these timescales.

The two 5.5 m beams of the telescope cease to intersect at a height of 853 m for the angle of 22.′16. For cloudlets moving through the beams, a characteristic speed of 1 m s^{-1} transports the fluctuations through the beams on a timescales of 5 s at this height. The 500 Hz switching "freezes" these fluctuations, which then cancel if they move through both the ANT and REF beams. We expect these fluctuations to cause an increased noise level in the second difference measurements.

The basic measurement is the "FLUX" (see Readhead et al. 1989 or Myers, Readhead, & Lawrence 1993 for a description of this procedure). In a FLUX measurement, the telescope first moves (slew time τ_s) to a position where the REF beam is pointed at the cluster (position "ON") and the ANT beam is 22.′16 away in azimuth (position "R1"), where it spends time τ_i integrating. The single-differenced

power recorded in this position is denoted "*A*." The telescope is then moved (τ_s again) so that the ANT beam points at the cluster ("ON" again) and the REF beam is displaced by 22.′16 in the opposite direction (position "R2") from the initial ANT position. Two consecutive integration cycles are performed in the new position, yielding power measurements "*B*" and "*C*." Finally, the telescope is moved back to the original position for an additional integration, denoted "*D*." If a series of FLUX measurements is to be performed consecutively on the same target, the subsequent "*A*" integrations are started from the same position as the previous "*D*" integration, without a telescope slew. Therefore, each FLUX beyond the first in a series takes a total time

$$\tau_f = 4\tau_i + 2\tau_s \,, \tag{1}$$

with the first FLUX in the series taking τ_s longer for the first slew. Typically, $\tau_s = 12$ s and $\tau_i = 20$ s, so a FLUX lasts $\tau_f = 104$ s. The actual slew time τ_s depends upon the zenith angle of the observation, increasing from 12 s for zenith angles greater than 30° to more than 30 s close to the zenith.

The individual integrations are normalized and calibrated such that they measure the antenna temperature differences $\langle T_{\rm ANT} - T_{\rm REF} \rangle$. We therefore construct an individual FLUX measurement

$$\mathrm{FLUX} = \tfrac{1}{4}(-A + B + C - D) \,. \tag{2}$$

The telescope also records a standard deviation (SD) measurement for each FLUX by measuring the variance of the 1 s difference measurements during the integrations. This procedure subtracts the average of the signals in two reference positions on either side of the cluster from the signal on the cluster. In terms of antenna temperature on the sky,

$$\mathrm{FLUX} = T_{\rm ON} - \tfrac{1}{2}(T_{R1} + T_{R2}) \,. \tag{3}$$

We can also rearrange the individual integrations *A*–*D*, which are recorded separately as part of the data log, to form other quantities of interest. For example, we define the *switched difference*

$$\mathrm{SW1} = \tfrac{1}{4}(-A - B + C + D) \,. \tag{4}$$

Because the differences $(D - A)$ and $(C - B)$ appear in the SW1, and are the integrations at the same position, the signal from the sky in the far field is cancelled, leaving only time variations of the atmosphere (possibly drifting through the slightly divergent beams), and spurious signals not common to the integration pairs. There is another combination of the integrations that cancels out the far-field signal,

$$\mathrm{SW2} = \tfrac{1}{4}(-A + B - C + D) \,, \tag{5}$$

which also acts like a time-difference filter, but with twice the frequency of the SW1. The more moderate filtering provided by the SW1 has proved to be a useful diagnostic for periods of bad data, without any bias due to strong celestial sources in the beams. Note also that, because of the form of equations (4) and (5), the SD from the FLUX applies to these quantities also. However, unlike the FLUX, the SW1 and SW2 are only single differences in time and tend to have correspondingly larger scatter about the mean values than the FLUXes. These quantities are useful for throwing out grossly discrepant measurements but do not provide a stringent filter for more subtle problems.

As the telescope tracks the cluster across the sky, the reference beams trace circular arcs around the cluster. The reference beams are always separated from the ON beam purely in azimuth. The position of the reference beams for a given FLUX is recorded in the form of the parallactic angle (ψ), defined as the angle between the direction of the north celestial pole and the direction of the zenith. The parallactic angle is

$$\tan\psi = \frac{\cos\lambda \sin H}{\sin\lambda \cos\delta - \cos\lambda \sin\delta \cos H} \,, \tag{6}$$

where λ is the geographic latitude of the telescope (37°13′, 55.″7 in the case of OVRO), δ is the declination of the object, and H is the hour angle. For objects transiting north of the zenith ($\delta > \lambda$), $\psi = 180°$ at transit, while $\psi = 0°$ at transit for $\delta < \lambda$. The position angles of the reference beams relative to the cluster are $\pm 90°$ away from the parallactic angle at the given time.

The reference beams are (very nearly) symmetric, so that we can fold the parallactic angle ψ into the range $(-90°, +90°)$ by adding or subtracting 180° with no loss of information. We define the principal parallactic angle (ψ_p) in this way. It is desirable for the observing time on a cluster to be as evenly distributed as possible over a large range of principal parallactic angle, since this makes it easier to identify contaminating sources in the reference beams. However, clusters that transit near the zenith spend the majority of their time at the extremes of their ψ_p range. The 7.′35 beam FWHM at the switching separation of 22.′16 subtends $\Delta\psi_p \sim 19°$; this is the effective "resolution" in parallactic angle.

3.2. *Lead-Trail Referencing*

The first and second levels of switching produce a FLUX measurement that is a "double difference": the difference between the signal in a central 7.′35 FWHM beam and the average of two reference beams 22.′16 on either side of the central beam. However, even with this differencing, offsets in the FLUX levels remain at the ~ 100 μK level. These offsets change as the telescope tracks a cluster; therefore, we must impose another level of differencing to remove this systematic effect.

The third level of switching involves observations of LEAD and TRAIL control fields far from the cluster centers. The LEAD and TRAIL fields are offset by $\pm\delta\alpha$ in right ascension from the cluster. Observations of the LEAD, MAIN, and TRAIL fields are separated by $\delta\alpha$ minutes in time so that the telescope tracks through the same azimuth and zenith angles for each field. This referencing was used in the Coma observations of Herbig et al. (1995). From each MAIN FLUX, we subtract the average of the LEAD and TRAIL FLUXes to form the referenced field M − [L + T]/2. This level of switching corrects for offsets dependent upon telescope orientation such as curvature in the ground spillover. We generally choose $10 \leq \delta\alpha \leq 25$ minutes, which is large enough so that the efficiency of the observations is not greatly reduced by frequent slewing but small enough that temporal variations in the offsets are not severe. Though essential for the removal of systematic errors, the three-level switching technique employed greatly reduces the efficiency of our observations. Only one-sixth of the observing time is

actually spent on the clusters, while the remainder is spent on the reference arcs and control fields.

The criterion for selecting $\delta\alpha$ is that both LEAD and TRAIL fields should be free of confusing radio sources bright enough to adversely affect the observations. We avoided sources found in the 4.85 GHz Green Bank survey (Gregory & Condon 1991). For clusters with $\delta\alpha = 15$ minutes, a typical scan consisted of six FLUXes on each of the LEAD, MAIN, and TRAIL fields. Each FLUX had a total integration time $4\tau_i = 92$ s. Fewer FLUXes could be completed per 15 minute scan near the zenith because of the increased slew time there. The cluster A478 was observed with $\delta\alpha = 19$ minutes, which allowed 10 FLUXes per scan with integration time $4\tau_i = 68$ s. Approximately 3 minutes per scan were allocated for calibration and slewing. To ensure complete parallactic angle coverage for all three fields, observations were scheduled in different LST blocks. These different schedules filled in gaps that would have been created if the telescope had been slewing at the same LST in every schedule. The pointing positions (J2000) used for the cluster LEAD, MAIN, and TRAIL fields in the observations are listed in Table 2.

3.3. *Calibration*

Calibration of the telescope and receiver was conducted regularly during the period from 1993 to 1995, with the most exhaustive calibration measurements taken in 1995. We derive our calibration scale from the 1995 data and apply it to our SZE data taken in 1993–1994 using observations of standard sources.

The telescope records the differenced power measurements for each FLUX in units of counts. In addition, the power from a calibrated noise diode is measured once at the end of each scan to normalize the changing gains in the system. The noise diode is calibrated in antenna temperature units by comparing its power output with hot (300 K) and cold (77 K) loads filling the beams, and in flux density units (1 Jy $= 10^{-23}$ ergs cm^{-2} s^{-1} Hz^{-1}) by comparing against "standard" radio sources such as Jupiter, Mars, and DR 21.

In addition to the waveguide switch that switches between the ANT and REF horns, the 5.5 m receiver has an additional switch in each of the ANT and REF arms that allows us to switch between the horn and a cold load as inputs (SKY and LOAD). The value of the CAL is measured with both arms looking at the loads, since this improves the stability of the measurement.

TABLE 2

POINTING POSITIONS FOR SZE OBSERVATIONS

	FIELD POSITION (J2000)	
CLUSTER	R.A.	Decl.
A478L	03:54:25.01	+10:27:40.73
A478	04:13:25.01	+10:27:40.73
A478T	04:32:25.01	+10:27:40.73
A2142L.....	15:43:18.00	+27:13:32.00
A2142	15:58:18.00	+27:13:32.00
A2142T.....	16:13:18.00	+27:13:32.00
A2256L.....	16:48:54.50	+78:38:27.00
A2256	17:03:54.50	+78:38:27.00
A2256T.....	17:18:54.50	+78:38:27.00

NOTE.—Units of right ascension are hours, minutes, and seconds, and units of declination are degrees, arcminutes, and arcseconds.

For each FLUX measurement, we assign a CAL value by linearly interpolating between the CAL measurements made before and after each FLUX. However, we do not use a CAL value if its standard deviation is greater than 5% of its value. This criterion rejects only about 1% of the CALs. We also do not use data if the difference between the bracketing CALs is greater than 5% of the mean value. Each FLUX and SD (standard deviation) measurement is divided by its assigned CAL value and multiplied by the appropriate temperature equivalent $T_{\rm cal}$ to yield antenna temperature.

The receiver system is slightly nonlinear. This nonlinearity has been measured and shown to be stable. Herbig (1993) has modeled the nonlinearity by assuming that the observed output power difference and the true input power difference are related by a linear function of the observed power. Because the CAL measurements are made with the load switches in the LOAD position while the FLUX measurements are made with the switches in the SKY position, a correction must be made for the nonlinearity difference between the two power levels. We use the average total power, which is recorded once during each scan with the antenna looking first at the sky and then at the load, to correct the CAL value to the power level of the FLUX measurement. Since the power levels change somewhat over the course of the observations, the correction must be applied to each FLUX individually. For the data set as a whole, over a range of zenith angles and atmospheric noise levels, the correction factor ranged from 0.96 to 1.00.

The aperture and beam efficiencies of the antenna are determined by comparing the flux densities of "standard" sources to the measured antenna temperatures. Measurements of Jupiter, Mars, DR 21, NGC 7027, and 3C 286 were made with the 5.5 m 32 GHz system during the period 1995 February–June. The flux density scale adopted for the 32 GHz observations is based upon a physical temperature of $T_{\rm J} = 144 \pm 8$ K (Wrixson, Welch, & Thornton 1971) for Jupiter at this frequency. This value encompasses the various measured temperatures for Jupiter, which range from 137 to 153 K. DR 21 and Mars are used as secondary calibrators. DR 21 is an H II region in the Galactic plane, and the 5.5 m measurements are confused by emission in the reference beams. The measured flux of DR 21, relative to Jupiter assuming $T_{\rm J} = 144$ K, is $S_{\rm DR\,21} = 19.4 \pm 0.3$ Jy, in agreement with 19.4 Jy measured by H. D. Aller (private communication), though not with the 18.2 Jy value given by the Baars scale (Baars et al. 1977). We also measure a temperature of Mars relative to Jupiter giving $T_{\rm M} = 180 \pm 3$ K. The flux densities of the planetary nebula NGC 7027 and of the radio galaxy 3C 286 were also measured relative to DR 21. We find $S_{\rm 3C\,286} = 1.92 \pm 0.06$ Jy for $S_{\rm DR\,21} = 19.4$ Jy. Note that NGC 7027 is expanding, and during 1995 February–June $S_{\rm N7027} = 5.10 \pm 0.14$ Jy. The scale is listed in Table 3, both relative to Jupiter and using the adopted absolute value $T_{\rm J} = 144$ K.

The equivalent flux density and thermodynamic load temperature for the CAL diode are related by

$$\frac{S_{\rm cal}}{T_{\rm cal}} = \frac{2k}{A_p \eta_A} = \frac{116.8 \text{ Jy K}^{-1}}{\eta_A}, \quad (7)$$

where the physical area A_p of the 5.5 m telescope is 23.64 m^2. Using the $T_{\rm J} = 144$ K flux density scale and measurements of the standard sources and hot and cold loads in

TABLE 3

OVRO 5.5 METER STANDARD CALIBRATION SCALE

Scale	$T_{\rm Mars}$	$S_{\rm DR\ 21}$	$S_{\rm N7027}$	$S_{\rm 3C\ 286}$
Relative to Jupiter.....	1.252 ± 0.022	134.7 ± 2.1 mJy K^{-1}	35.5 ± 1.1 mJy K^{-1}	13.2 ± 0.6 mJy K^{-1}
$T_{\rm Jupiter} = 144 \pm 8$ K.....	180 ± 10 K	19.4 ± 1.1 Jy	5.11 ± 0.33 Jy	1.90 ± 0.14 Jy

1993 April, 1993 June, 1994 October, and 1995 April, we calculate the aperture efficiency of the 5.5 m telescope to be $\eta_A = 0.497 \pm 0.007$ (4.255 ± 0.014 mK Jy^{-1}). The CAL temperature $T_{\rm cal}$ corresponds to the equivalent Rayleigh-Jeans temperature increase in a blackbody filling the entire telescope beam. Because the power output of the CAL diode has been found on occasion to vary on timescales of months, the equivalent temperature or flux density of the CAL must be determined for the time period of calibration. During the SZE observing sessions from 1993 July to 1994 April, the ratio of DR 21 to the CAL was measured to be 0.1542 ± 0.0022. The stated uncertainty is the standard deviation about the mean for 12 observations spread over this interval and should reflect the range of possible variation in the CAL over this period. From these measurements, we deduce that the CAL was stable to at least 1.4% rms. Assuming a flux density of 19.4 Jy for DR 21, we adopt a constant value of $S_{\rm cal} = 125.8 \pm 1.8$ Jy, which corresponds to $T_{\rm cal} = 535 \pm 11$ mK. After normalizing our FLUX values by the CAL, we multiply by $T_{\rm cal}$ in order to compare the measurements with the expected thermal noise.

The relationship between the flux density and measured antenna temperature of a source filling the main beam of the telescope is

$$\frac{S_\nu}{T_a} = \frac{2k}{\lambda^2}\,\Omega_{\rm mb} = 161 \pm 4 \text{ Jy K}^{-1} \tag{8}$$

for the measured main beam solid angle $\Omega_{\rm mb} = (5.12 \pm 0.14) \times 10^{-6}$ sr and observing wavelength $\lambda = 0.938$ cm. Note that equations (7) and (8) differ by

$$\frac{\eta_B}{\eta_A} = \frac{A_p \Omega_{\rm mb}}{\lambda^2} = 1.38 \pm 0.04\,, \tag{9}$$

where η_B is the fraction of the entire telescope beam in the forward main beam. From the aperture efficiency and main beam solid angle, we derive a beam efficiency $\eta_B = 0.684 \pm 0.021$. A radio source of flux density $S_{\rm cal}$ is equivalent to a source filling the main beam with uniform Rayleigh-Jeans brightness temperature

$$T^*_{\rm cal} = \frac{\lambda^2}{2k\Omega_{\rm mb}}\,S_{\rm cal} = \frac{T_{\rm cal}}{\eta_B} = 782 \pm 24 \text{ mK}\,. \tag{10}$$

This is the appropriate CAL value to use for calibrating the astronomical signal in the main beam. The FLUX measurements, already scaled by $T_{\rm cal}$, must be divided by the beam efficiency η_B to effectively scale by $T^*_{\rm cal}$.

The FLUX and SD values must also be scaled by a factor that accounts for atmospheric attenuation. Atmospheric attenuation reduces the intensity by a factor $\approx e^{-a \sec \theta_Z}$, where θ_Z is the zenith angle and a is the optical depth. In good weather at $\nu = 32$ GHz, $a \sim 0.04$ (assuming $a \sim T_{\rm atm}/T_{\rm phys} \approx 11$ K/270 K). The estimated rms variation in the atmospheric optical depth is $\sigma_a \lesssim 0.02$, based upon water-vapor radiometry data obtained at OVRO.

In summary, the raw FLUX and SD values are first divided by the CAL value, then scaled by the CAL temperature $T_{\rm cal}$. After editing, the measurements are scaled by the correction factor:

$$\kappa = \frac{e^{a \sec \theta_Z}}{\eta_B} = 1.46 e^{0.04 \sec \theta_Z}\,. \tag{11}$$

At this stage, the measurements are in kelvins and are equivalent to the differences in temperature between two high-temperature uniform blackbody emitters (calculated using the Rayleigh-Jeans formula) filling the main beams of the ANT and REF horns that would produce the observed power differences.

The total calibration uncertainty is the quadrature sum of the uncertainties in (1) the temperature of Jupiter T_J (5.6%), (2) the ratio of our measured flux of DR 21 relative to Jupiter (1.6%), (3) the ratio of the CAL $S_{\rm cal}$ to DR 21 during the course of the observations (1.4%), (4) the main beam solid angle converting flux density to brightness temperature (2.7%), and (5) the atmospheric attenuation variation (2.0%), giving a total calibration error budget of 6.9%. The dominant uncertainty is the absolute brightness temperature of Jupiter. The relative flux density scale, (2) and (3), is accurate to 2.1%, while the temperature scale, (2), (3), and (4), is accurate to 3.4% (without atmospheric correction). For improvement in the SZE measurements beyond what is reported here, a more accurate absolute flux density scale at 32 GHz is required.

3.4. *Data Editing*

Many of the data taken during the afternoon or when the weather was bad was clearly unusable, and a method of editing the data without introducing any systematic biases had to be devised. The two general editing methods used were editing based on the SD values and filtering based on the standard deviation of the switched difference measurements.

Before applying these methods, we removed FLUXes for which the elapsed time exceeded the expected duration by more than 4 s. Excessive durations could be caused by extremely high winds or tracking problems that would corrupt the data. In addition, on several occasions, problems arose with the zenith angle encoder that caused the drive to fail and that resulted in a few extremely long FLUXes during which the telescope was not tracking the source.

The procedure for thermal editing is based upon the expected thermal noise in a FLUX measurement. The thermal standard deviation is given by

$$\sigma_{\rm th} = \frac{2T_{\rm sys}}{\sqrt{4\tau_i\,\Delta\nu}} = \frac{T_{\rm sys}}{\sqrt{\tau_i\,\Delta\nu}}\,, \tag{12}$$

where $4\tau_i$ is the total integration time of the FLUX, $\Delta\nu = 5.7$ GHz is the bandwidth of TRW amplifier, and the

numerical factor arises because of the double switching inherent in the FLUX measurement and the FLUX definition of equation (2). The system temperature T_{sys} is given by

$$T_{sys} = T_0 + T_{atm} \sec \theta_Z. \tag{13}$$

T_{atm} is the atmospheric emission temperature per air mass. Included in T_0 are contributions from the receiver, the ground, and the 2.726 K cosmic background (Mather et al. 1994):

$$\begin{aligned} T_0 &= T_{rx} + T_{gnd} + 2.726 \text{ K} \\ T_{rx} &= 33.0 \pm 1.6 \text{ K} \\ T_{gnd} &\approx 8 \text{ K} \\ T_{atm} &\sim 10 \text{ K} . \end{aligned} \tag{14}$$

At one air mass for $\tau_i = 20$ s, this gives $\sigma_{th} = 0.16$ mK. Even with the overhead from the three-level switching, we would expect to integrate down to a noise level of around 36 μK in the referenced field M − [L + T]/2 in about 3 hr of total integration time. In practice, additional atmospheric noise not removed by the double differencing increases the noise significantly above this level.

We first wish to reject blocks of data that are clearly contaminated by bad weather. Our method is a modification of the method developed by Brandt (1992), in which one searches for blocks of good data that contain a specified number of points, typically 10–25, within a limited time range, typically 2 hr. Sliding buffers are moved over the data set, and any point that is contained within a "good" block of data is accepted.

For each point i in the data set, we construct the "test" statistic

$$t_i = X_i/\sigma_{th,i} . \tag{15}$$

We have divided the value by the corresponding thermal noise level $\sigma_{th,i}$ to account for the increased scatter expected at high zenith angle, where the telescope is looking through a longer column of air, and to allow comparison of data points with differing integration times. The value X used as the statistic can be FLUX, SD, SW1, or SW2.

The test values are placed into "buffers" of N consecutive points, for which the mean and the standard deviation about the mean are calculated. For buffer j,

$$\bar{t}_j = \frac{1}{N} \sum_{i=j}^{j+N-1} t_i \tag{16a}$$

$$s_j = \left[\frac{1}{N} \sum_{i=j}^{j+N-1} (t_i - \bar{t}_j)^2 \right]^{1/2} . \tag{16b}$$

Each test buffer contains N points, restricted to be taken over a maximum span of not more than 2 hr.

The filter was applied by examining all buffers that contain a given data point i. A data point i is rejected if there exists no buffer j of the chosen length N containing the given point for which the standard deviation s_j is less than a chosen cutoff value s_{max} and for which the mean $\bar{t}_j$ is less than a limit $\bar{t}_{max}$. We used either the mean or the standard deviation of the test values X in the filter, but not both at once. We designate these filters as "meanX[N, $\bar{t}_{max}$]" or "sigX[N, s_{max}]." In addition, we can simply throw out discrepant values with $t_i > t_{max}$, with filter designation "X[t_{max}]." This brute force rejection is useful only for the SD, where it can remove single points with large error bars that escape previous filters. In these filters, the FLUX values themselves are not used to avoid bias of the results.

Through experimentation upon the data, we have developed a filtering sequence that produces good results and is robust to slight changes in the filter parameters:

1. Filter on mean of SD, with $N = 25$ and $\bar{t}_{max} = 2.0$ (mean SD [25,2.0]).
2. Reject points with high SD, using $t_{max} = 2.5$ (SD[2.5]).
3. Filter on standard deviation of SW1, with $N = 10$ and $s_{max} = 7.5$ (sigSW1[10, 7.5]).

After our filtering, we are left with a "clean" distribution of FLUXes, although a few FLUXes with discrepant values from the mean may remain. These points can escape our culling procedure if they are due to stationary structures in the far-field atmosphere or, of course, spurious noise or interference that happens to mimic the switching scheme of the FLUX (unlikely, but possible). The removal of "bad" FLUXes that show no ill effects in the respective SW1, SW2, or SD without biasing the data is a tricky business. A conservative approach would be to reject all FLUXes that are part of a scan on a given field for which the standard deviation of the FLUXes about the scan mean is above some limit—this should be equivalent to a noise level edit. In practice, we will use the scan standard deviations to downweight this data during the analysis (see next section).

Our approach, one we have adopted with success in the past (Readhead et al. 1989; Myers et al. 1993), is to throw out the FLUXes on the tail of the FLUX distribution for a given field using an iterative procedure to ensure that the resulting postedit distribution is not skewed by applying too stringent a cutoff. This rejection procedure we designate as "rejX[σ]." For the cluster data, we reject iteratively the *referenced* temperatures ΔT_{MLT} (see below) with a cutoff of 4 σ (rejMLT[4]). Note that for reasonable cutoffs ($> 3\ \sigma$), this procedure will not introduce a bias into the data, since outliers are rejected one at a time and after each iteration the mean and standard deviation are recalculated.

Discussion of the effects of different editing and filtering parameters will be presented in the next section.

3.5. *Analysis of SZE Measurements*

Software was designed to perform the subtraction of the reference LEAD and TRAIL fields from the MAIN field. The program first multiplies the filtered and edited data by the correction constant κ from equation (11)

$$\Delta T_i = \kappa \text{FLUX}_i \quad \sigma_i = \kappa \text{SD}_i \tag{17}$$

to convert the power differences into Rayleigh-Jeans temperature differences in kelvins between the ANT and REF main beams. The separate FLUXes from the adjacent MAIN (M), LEAD (L), and TRAIL (T) scans are then matched based on their proximity in the azimuth and zenith coordinates. The FLUXes in the MAIN fields are matched with the closest FLUXes in the adjacent LEAD and TRAIL fields that have not already been matched to other MAIN points. Matching LEAD and TRAIL measurements are required for each MAIN—if no reference FLUXes are found in the LEAD or TRAIL that are closer than 5′ (a substantial fraction of the beam width) from the MAIN field, the MAIN FLUX is discarded. For each triplet, we

calculate the "referenced" differences

$$\Delta T_{\rm MLT} = \Delta T_{\rm M} - \tfrac{1}{2}(\Delta T_{\rm L} + \Delta T_{\rm T}) \quad (18a)$$

$$\Delta T_{\rm M-L} = \Delta T_{\rm M} - \Delta T_{\rm L} \quad (18b)$$

$$\Delta T_{\rm M-T} = \Delta T_{\rm M} - \Delta T_{\rm T} \quad (18c)$$

$$\Delta T_{\overline{\rm LT}} = \tfrac{1}{2}(\Delta T_{\rm L} + \Delta T_{\rm T}) \quad (18d)$$

$$\Delta T_{\rm L-T} = \Delta T_{\rm L} - \Delta T_{\rm T} \, . \quad (18e)$$

Gaussian error propagation is used to compute the statistical uncertainties in these differences. For example,

$$\sigma^2_{\rm MLT} = \sigma^2_{\rm M} + \tfrac{1}{4}(\sigma^2_{\rm L} + \sigma^2_{\rm T}) \, . \quad (19)$$

The referenced points are then weighted and the statistics are formed. For each of the N points with M − [L + T]/2 , M − L , M − T , etc., we form $\overline{\Delta T} \pm \epsilon$, where

$$\overline{\Delta T} = \frac{1}{W_1} \sum_{j=1}^{N} w_j \Delta T_j \quad (20a)$$

$$\epsilon^2 = \frac{W_2}{W_1^2} \sigma^2 \quad (20b)$$

$$\sigma^2 = \frac{N}{N-1} \frac{1}{W_2} \sum_{j=1}^{N} w_j^2 (\Delta T_j - \overline{\Delta T})^2 \quad (20c)$$

$$W_1 = \sum_{j=1}^{N} w_j \quad (20d)$$

$$W_2 = \sum_{j=1}^{N} w_j^2 \, . \quad (20e)$$

The weights are formed from a combination of the individual errors σ_j (e.g., eq. [17]) and the standard deviation of the points within scans $\sigma_{\rm sc}$,

$$w_j^{-1} = a_0 + a_1 \sigma_j^2 + a_2 \sigma^2_{{\rm sc},j} \, . \quad (21)$$

The standard deviation SD recorded with each FLUX generally underestimates the actual error by a factor of 2 or 3. This is a result of atmospheric fluctuations on a timescale longer than the duration of the FLUXes. A better estimate of the true error is the scatter of the FLUX measurements within a scan. An appropriate weighting is $a_1 = a_2 = 1$ and $a_0 = 0$. The inclusion of the individual SDs $a_1 \neq 0$ guards against anomalously low scan standard deviations causing very large weights, while the weight will normally be dominated by the larger scan standard deviations $\sigma_{{\rm sc},j}$.

Figure 1 shows our results for A478, A2142, and A2256 using 20 different filtering methods. The referenced measurements $\Delta T_{\rm MLT}$ are plotted. Both unweighted (u: $a_0 = 1$, $a_1 = a_2 = 0$) and weighted (w: $a_1 = a_2 = 1$, $a_0 = 0$) results are shown. The methods are enumerated by filtering and outlier editing schemes. There were five filtering methods chosen:

Method 1.—No filtering.
Method 5.—SD[3.0].
Method 9.—meanSD[25, 2.5], SD[3.0].
Method 13.—meanSD[25, 2.0], SD[2.5], sigSW1[10, 7.5].
Method 17.—meanSD[25, 1.5], SD[2.0], sigSW1[10, 6.0].

In addition, for each filter, four different outlier rejection schemes were tested:

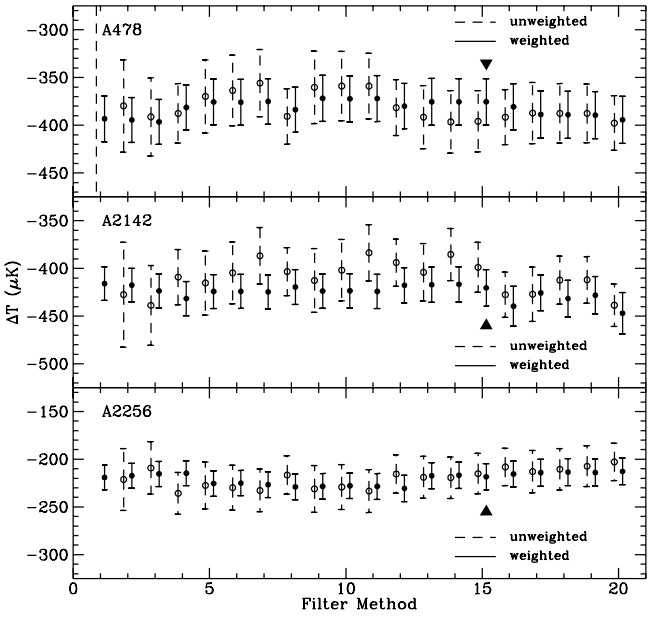

FIG. 1.—Effect of the data editing and filtering method upon the final referenced results. We show results for 20 different editing methods, for both unweighted (*dashed lines*) and weighted (*solid lines*) averages. The points are plotted slightly displaced from the filter method. The methods are roughly in order of fraction of data accepted, ranging from 100% (method 1) to 44% (method 20). The effective fraction of data used in the weighted averages ranges from 37% to 27% across the filter methods. We adopt method 15 with weighting (marked with the triangle), in which 57% of the data is retained, with an effective weighted fraction of 31%.

Method n + 0.—No outlier editing.
Method n + 1.—rejMLT[5] (5 σ rejection).
Method n + 2.—rejMLT[4] (4 σ rejection).
Method n + 3.—rejMLT[3] (3 σ rejection).

These filter methods 1–20 are roughly in increasing order of fraction of the data rejected. A total of 802.5 hr of MAIN, LEAD, and TRAIL data were passed with no filtering, editing, or weighting (Method 1u), while only 351.7 hr of data were accepted for Method 20u.

For the weighted means, the form of equation (20*a*) suggests an effective number of points

$$N_{\rm eff} = \frac{W_1^2}{W_2} = \left(\sum_{j=1}^{N} w_j \right)^2 \Big/ \sum_{j=1}^{N} w_j^2 \, . \quad (22)$$

The effective fraction ($\sim N_{\rm eff}/N$) of accepted data ranges from 35% (Method 1w) to 27% (Method 20w) with little variation between outlier editing modes for each filter method. Note the smaller variation between the weighted methods; the weighting largely takes care of the editing by down-weighting bad stretches of data. The unedited and unweighted data point (Method 1u) is not visible in Figure 1, as it is heavily corrupted by bad data and is off scale. The corresponding weighted point (Method 1w) is consistent with the other data points.

We adopt Method 15w: meanSD[25, 2.0], SD[2.5], sigSW1[10, 7.5] filtering, rejMLT[4] outlier editing, and weighting $a_1 = a_2 = 1$, $a_0 = 0$ (marked in Fig. 1). Because none of the results differ significantly with respect to the statistical error bars, we are confident that even fairly large differences in the filtering method have negligible effect upon our results. We conclude that our automatic editing procedure is reliable and robust.

4. SZE RESULTS

In all three clusters, A478, A2142, and A2256, we find significant detections of a microwave decrement that we attribute to the SZE. Table 4 lists the measured values of ΔT for these clusters. In addition to the fully referenced difference M − [L + T]/2 , and the single-referenced differences M − L and M − T , we also list the averages for each of the MAIN, LEAD, and TRAIL fields separately, as well as the weighted difference and average of the LEAD and TRAIL. If there is no significant source contamination, we expect the averaged L − T to be consistent with zero, provided that our switching technique is subtracting all significant ground spillover effects. However, if ground spillover or atmospheric emission varies with a timescale shorter than the time between the MAIN, LEAD, and TRAIL scans, the L − T may be inconsistent with zero, but this effect could be expected to average out over the course of an observing season. Source contamination in the control fields will generally result in nonzero values for L − T and will contaminate the average (L + T)/2.

The measurements of the SZE as a function of principal parallactic angle ψ_p are presented in Figures 2, 3, and 4. The upper panels of each plot show the individual MAIN, LEAD, and TRAIL binned averages, while the lower panels show the referenced M − [L + T]/2 and L − T. The scatter of these referenced values with parallactic angle can give an estimate of possible reference arc contamination.

For A478, we find $\Delta T = -375 \pm 24$ μK with 64 total hr of integration time, a 15.6 σ detection. Figure 2 shows ΔT binned by parallactic angle ψ_p. The close agreement of the LEAD and TRAIL over the entire range of ψ_p suggests that there is no significant source contamination of the control fields. Although the M − [L + T]/2 is nearly constant with ψ_p, with $\chi^2 = 1.70$ about the mean in the five bins, the individual fields in the upper figure show variations of $\sim$400 μK resulting from ground spillover. This demonstrates the necessity of our LEAD and TRAIL referencing. The LEAD and TRAIL difference L − T is consistent with zero and has $\chi^2 = 6.87$ about zero in the five parallactic angle bins, which is significant only at the 79% level. Thus, we conclude that there is no evidence for source contamination in the A478 data.

A microwave decrement of $\Delta T = -420 \pm 19$ μK is found in A2142, a detection significant at the 22 σ level. There were 85 hr of usable integration time on this cluster. As shown in Figure 3, the LEAD and TRAIL track each other with an average offset of 188 μK. There is a mean L − T difference of -66 ± 20, which is marginally significant at the 3 σ level. In Figure 3, we see a feature in the L − T at parallactic angle $\psi_p \sim -20°$. This is consistent with a source in the LEAD reference arc centered at $\psi_p = -21°$ (see next section). The χ^2 is 3.14 about zero in the four parallactic angle bins, although since most of the data are at

TABLE 4

OVRO 5.5 METER MEASUREMENTS OF SZE

Parameter	A478 (μK)	A2142 (μK)	A2256 (μK)
M − (L + T)/2.....	-375 ± 24	-420 ± 19	-218 ± 14
M − L.....	-366 ± 27	-399 ± 20	-217 ± 15
M − T.....	-386 ± 27	-451 ± 22	-238 ± 16
MAIN.....	-139 ± 20	-214 ± 17	-310 ± 12
LEAD	244 ± 21	159 ± 17	-94 ± 12
TRAIL	242 ± 20	226 ± 16	-82 ± 12
L − T.....	-13 ± 27	-66 ± 20	-22 ± 15
(L + T)/2.....	248 ± 15	188 ± 13	-74 ± 13
$\nu_{\rm eff}$	800	840	2020
$n_{\rm pts}$	1146	1337	4117
τ (hr).....	64	85	310

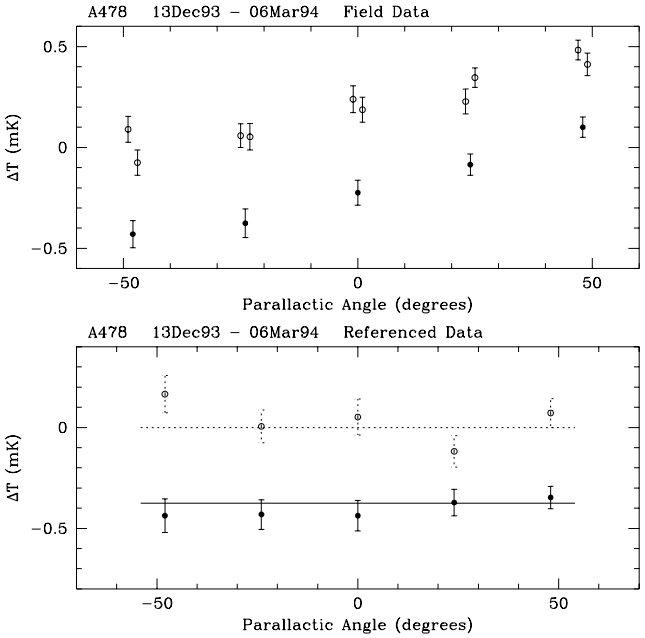

FIG. 2.—Dependence of the LEAD, MAIN, and TRAIL (*upper*) and MLT and L-T referenced data (*lower*) on parallactic angle are shown for A478. In the upper panels, the LEAD fluxes are offset to the left of the proper ψ_p, and the TRAIL fluxes are offset to the right. In the lower panel, the solid and dotted horizontal lines depict the means of the MLT and L-T. No source contributions were subtracted from A478.

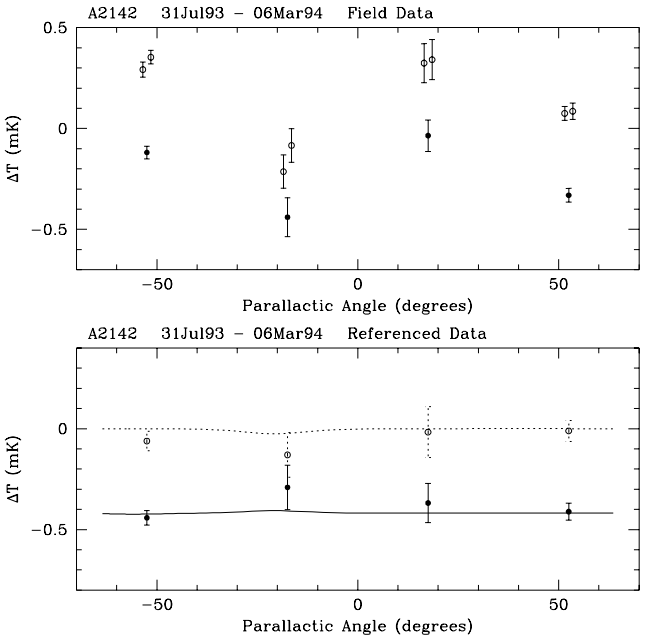

FIG. 3.—Dependence of the LEAD, MAIN, and TRAIL (*upper*) and MLT and L-T referenced data (*lower*) on parallactic angle are shown for A2142. In the lower panel, the solid and dotted horizontal curves represent response of the MLT and L-T data to the contaminating sources. Note the signal at $\psi_p = -21°$ that matches the deviation in the data. The expected signal from the source is below that observed, and we may have underestimated its contribution. However, because the number of data points in this ψ_p range is small, this does not affect the results significantly.

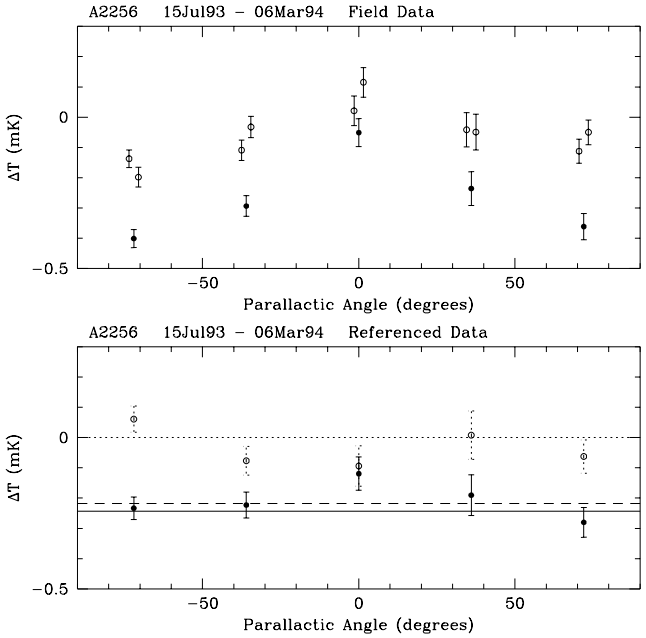

FIG. 4.—Dependence of the LEAD, MAIN, and TRAIL (*upper*) and MLT and L-T referenced data (*lower*) on parallactic angle are shown for A2256. In the lower panel, the dotted horizontal line depicts the expected zero mean L-T, as no scans of these fields were available. The dotted line is the MLT mean before main beam source correction, and the solid line is the mean after source correction.

the ends of the arcs, the effective number of degrees of freedom (eq. [22]) is only 2.7. The significance of this χ^2 value is 67%. The referenced M − [L + T]/2 has a χ^2 of 2.1 about the mean for 1.5 effective degrees of freedom, which is significant only at the 75% level.

We measure $\Delta T = -218 \pm 14$ μK for A2256, a detection significant at 15.6 σ. There were 310 hr of integration time on A2256. The MAIN, LEAD, and TRAIL data are shown binned by parallactic angle in Figure 4. Because A2256 is circumpolar, the magnitude of the average LEAD and TRAIL is somewhat smaller for this cluster as it traverses a more restricted range in azimuth and zenith angle and is not as strongly affected by changes in ground spillover as are A2142 and A478. The overall average difference between LEAD and TRAIL is again consistent with zero, -22 ± 15 μK. However, when the data are binned in parallactic angle as in Figure 4, we find $\chi^2 = 7.88$ versus zero for 4.3 effective degrees of freedom, which is significant at the 88% level. After referencing, the χ^2 of M − [L + T]/2 data versus the mean is 5.17 for 3.3 effective degrees of freedom, or 81% significance.

In all three cases, the MAIN field is clearly showing the SZE decrement relative to the LEAD and TRAIL, while all three track together with parallactic angle. The variation of the LEAD and TRAIL average offset with ψ_p shows the importance of the extra referencing to remove the differential ground spillover component. This referencing was also performed using a slightly different procedure in the Coma observations of Herbig et al. (1995).

The data set is also robust with respect to separating into different time periods and different times of day. No trends are seen that are significant compared to the statistical uncertainties.

After referencing, we have rms uncertainty levels of 14–24 μK. On these angular scales at this fluctuation level, anisotropies in the cosmic microwave background radiation itself can be expected to be detectable. Intrinsic fluctuations on this scale are expected to be in the range $5 \times 10^{-6} \lesssim \Delta T/T \lesssim 2 \times 10^{-5}$ (14–55 μK) in the most popular models (see, e.g., Bond et al. 1994). Our instrumental filtering can be expected to reduce the CMB anisotropy signal somewhat, as will the smearing with parallactic angle of the reference beams. The clearest indicator of CMB fluctuations would be significant L − T differences; the fact that we have no clear detection of a LEAD − TRAIL difference, except possibly in A2142, indicates that the true anisotropies are not much greater than the predicted range. In a separate observing program, we have conducted a microwave background anisotropy experiment using the 5.5 m telescope and the same instrumental configuration, the results of which will be reported in an upcoming paper. If the background fluctuations are indeed in the expected range, then pushing the SZE on these scales to much lower noise levels will not be possible using single-frequency measurements such as ours. Note, however, the SZE in more distant and hence much smaller angular-sized clusters will not be so badly affected, as the background fluctuations on smaller scales are expected to be considerably smaller.

A significant contribution to systematic error in the SZE measurements is foreground contamination by Galactic and extragalactic emission. At this frequency and angular scale, we believe that Galactic dust and free-free emission are not likely to be major contaminants. However, synchrotron emission by discrete extragalactic sources is known to be a significant problem.

5. SOURCE CONTAMINATION

An unfortunate aspect of centimeter-wavelength observations of the SZE is that they must contend with the presence of radio sources that can mimic or hide the effect. High-resolution radio maps must be made at or near the frequency of observation to deal effectively with this problem. Unfortunately, many radio sources are also variable, and if a cluster is contaminated by such sources, be they field object or associated with the cluster, simultaneous observations must be made on different telescopes. This was not feasible for the present work; however, previously published observations of the fields of many of our clusters suggest that our results are not greatly affected by source contamination. Note that in this respect, interferometric SZE observations are superior—the longer baselines provide the simultaneous high-resolution information necessary for source identification, and if the baselines extend far enough compared to the shortest spacings, a clean subtraction of the interfering sources can be made. However, with single-dish data, we have not this luxury.

Radio observations of adequate resolution for computing corrections to SZE measurements have been published for many of the clusters in our sample. However, these maps extend only about 20′ from the cluster centers, so the possibility exists that there are unrecognized contaminating sources in the reference arcs. For the LEAD and TRAIL fields, we use data from the 1987 Green Bank survey at 4.85 GHz (Gregory & Condon 1991), which lists sources down to a flux limit of 25 mJy. Unfortunately, the declination range of this survey does not include A2256, and the radio environments of the LEAD and TRAIL field for this cluster are at present unknown. However, the excellent match between the LEAD and TRAIL fluxes and the stability of

the referenced $\Delta T_{\rm MLT}$ with ψ_p give us confidence that contamination is not a serious problem in A2256. Many of the clusters in our sample fall below the southern declination limit of the Green Bank survey, and for these we obtained source positions from preliminary results of the southern Parkes-MIT-NRAO (PMN) survey (Griffith & Wright 1993).

5.1. *40 Meter Observations at OVRO*

The published observations of discrete radio sources have been carried out at frequencies considerably lower than our observing frequency of 32 GHz. For this reason, we observed the contaminating sources from the Green Bank and PMN surveys with the OVRO 40 m telescope at 18.5 GHz. We observed sources within $30^{\rm m}$ in right ascension and $32'$ in declination from the cluster center in order to cover the possible locations for the LEAD and TRAIL fields. Sources near the cluster centers were also identified from higher resolution radio maps. Images of A478 and A2142 at 2.7, 4.75, and 10.7 GHz were available (Andernach et al. 1986), as well as for A2256 at 610 and 1415 MHz (Bridle et al. 1979).

At a frequency of 18.5 GHz, the 40 m telescope has a beamwidth of $2'$ FWHM. Because of its larger collecting area and much higher sensitivity to point sources, the 40 m telescope can measure any sources that would be bright enough to affect 5.5 m SZE observations in a relatively short integration time. Observations of these confusing sources were carried out during the period between 1993 November 20 and 1994 January 24. Many observations were repeated several weeks after the initial observations in order to gauge variability.

The desired sensitivity level was achieved in around 400 s of integration time on each source. On the 40 m telescope, we use the same double differencing procedure in measuring FLUXes as on the 5.5 m telescope (§ 3.1). Pointing was checked before each scan on a source. Calibration was performed by observing DR 21, which has a flux of 19.2 ± 0.7 mJy at 18.5 GHz. Because of the large size of the 40 m telescope, physical deformation of the dish causes the gain to vary with elevation. Long tracks on 3C 84 were used to determine the zenith-angle–dependent gain corrections. We estimate the error for calibration and gain corrections at $\sim 6\%$, similar to those for the 5.5 m telescope.

The 40 m telescope 18.5 GHz measurements are listed in Table 5, along with the lower frequency flux density measurements ($S_{\rm low}$) at 4.85 GHz, 2.7 GHz, and 10.7 GHz obtained from the literature. Where the 18.5 GHz measurement was not significant at the 3 σ level, the 3 σ upper limit on the flux density is listed. The deduced spectral index α for each source, between the lower frequency and 18.5 GHz, are given, where a power-law spectrum is assumed

$$S \propto \nu^{\alpha} . \tag{23}$$

The extrapolated flux densities S_{32} are listed in the last column. These were calculated using the values for α listed in the table or from upper limits where appropriate.

Because the 18.5 GHz frequency of our source measurements is significantly lower than the 32 GHz observing frequency of our SZE data and also because we have no bracketing measurements at higher frequencies, one should conservatively assume the 18.5 GHz measurements themselves as an upper limit to the 32 GHz source flux densities. It is possible that the 18.5 GHz emission is dominated by flat-spectrum compact components in the radio sources. From the numbers in Table 5, we see that this leaves us with an overall factor of 2 uncertainty in the source corrections to be applied where a detection at 18.5 GHz was made. Only better measurements of these sources at frequencies bracketing 32 GHz will allow accurate source subtraction to be made.

5.2. *Corrections to SZE Measurements*

The radial distances and position angles (relative to north through east) of these contaminating sources relative to the field centers are given in Table 6. If the source lies within the

TABLE 5

SOURCES WITHIN 9′ OF FIELD CENTERS OR REFERENCE ARCS

SOURCE	POSITION (J2000) R.A.	POSITION (J2000) Decl.	$S_{\rm low}$ (mJy) [a]	$S_{18.5}$ (mJy)	α	S_{32} (mJy)
A478L.1	03:54:57.2	+10:12:30	33 ± 7	<3.9	< -1.4	<1.8
A478.1	04:13:34	+10:28:04	16 ± 7[b]	<9.1	<0.2	<9.2
A2142L.1	15:41:46.8	+27:05:54	51 ± 8	13.5 ± 1.1	-0.99 ± 0.13	7.8 ± 0.9
A2142L.2	15:42:58.4	+27:06:46	34 ± 7	<5.1	< -1.2	<2.6
A2142.1	15:57:11.2	+26:51:31	52 ± 9	8.5 ± 1.9	-1.35 ± 0.21	4.1 ± 1.1
A2142.2	15:58:14.3	+27:15:48	44 ± 8	7.9 ± 2.0	-1.28 ± 0.23	3.9 ± 1.1
A2142.3	15:58:47	+27:18:06	18 ± 7[c]	<6.3	< -0.3	<5.4
A2142.4	15:59:05	+27:03:19	42 ± 15[c]	<5.1	< -0.9	<3.2
A2142T.1	16:12:26.3	+27:23:16	49 ± 8	14.3 ± 1.5	-0.92 ± 0.14	8.6 ± 1.1
A2256.1	17:02:09	+78:40:56	48 ± 8[d]	<6.9	< -0.7	<4.8
A2256.2	17:02:28	+78:42:57	166 ± 1[d]	<4.8	< -1.3	<2.3
A2256.3	17:03:03	+78:36:40	62 ± 4[d]	<5.1	< -0.9	<3.0
A2256.4	17:03:09	+78:40:00	39 ± 3[d]	<6.0	< -0.7	<4.1
A2256.5	17:03:28	+78:37:58	157 ± 10[d]	8.3 ± 2.5	-1.14 ± 0.12	4.4 ± 1.4
A2256.6	17:03:51	+78:46:03	185 ± 13[d]	<10.8	< -1.1	<6.0
A2256.7	17:04:48.9	+78:38:29	11 ± 1[d]	<10.5	<0.03	<10.7

NOTE.—Units of right ascension are hours, minutes, and seconds, and units of declination are degrees, arcminutes, and arcseconds.

[a] Flux density at 4.85 GHz from 87GB unless otherwise noted.

[b] Flux density at 10.7 GHz (Andernach et al. 1986).

[c] Flux density at 2.7 GHz (Andernach et al. 1986).

[d] Flux density at 1.415 GHz (Bridle et al. 1979).

TABLE 6

CORRECTIONS FOR SOURCES WITHIN 9′ OF FIELD CENTERS OR REFERENCE ARCS

Source	Radius (arcmin)	Position Angle (deg)	d (arcmin)	ψ_p (deg)	ΔT_a (μK)	$\Delta T_{\max}$ (μK)
A478L.1	17.12	152	5.81	62	<11	<1
A478.1	2.24	80	...	...	<57	<44
A2142L.1.....	21.67	249	0.49	-21	48 ± 6	-24 ± 3
A2142L.2.....	8.05	213	...	...	<16	<1
A2142.1	26.57	214	4.41	-56	26 ± 7	-5 ± 1
A2142.2	2.41	340	...	...	24 ± 7	18 ± 5
A2142.3	7.90	55	...	...	<34	<1
A2142.4	14.62	134	7.54	44	<20	<1
A2142T.1.....	15.05	310	7.11	40	53 ± 7	-2.0 ± 0.3
A2256.1	5.75	296	...	...	<30	<5
A2256.2	6.19	317	...	...	<14	<2
A2256.3	3.10	235	...	...	<19	<11
A2256.4	2.72	305	...	...	<26	<17
A2256.5	1.39	250	...	...	27 ± 9	25 ± 8
A2256.6	7.60	359	...	...	<37	<2
A2256.7	2.68	89	...	...	<67	<46

NOTE.—Radius (arcmin) and position angle are measured from center of main field. Distance d (arcmin) is measured from center of reference arc at parallactic angle ψ_p.

reference beam arc 22.′16 away from the central beam, then the corresponding distance from the closest arc center r and the parallactic angle ψ_p of the closest approach are also listed. The implied equivalent SZE temperatures ΔT_a are calculated using 6.22 mK Jy^{-1}, since the SZE measurements have already been converted to main-beam temperatures (see eq. [8]). There is a 6.6% overall conversion uncertainty that includes all of the flux density scale uncertainties (see § 3.3), although this is less than the uncertainty in the source flux density extrapolation to 32 GHz and thus has not been applied to the numbers in Table 6. Finally, correction for the 7.′35 Gaussian beam pattern produces the expected maximum contributions $\Delta T_{\max}$ printed in the last column of the table.

In the MAIN fields, if a source falls within the central part of the main 5.5 m beam, it will tend to cancel out the SZE decrement. Sources in the reference arcs are *subtracted* and thus mimic a decrement, but they will be observed only at certain parallactic angles. Such sources are recognizable by their signature on a plot of the SZE decrement versus parallactic angle ψ_p. Sources in the beams of the LEAD and TRAIL fields will have the opposite effect compared to those in the MAIN field, with levels reduced by a factor of 2 owing to the averaging (M − [L + T]/2).

Because each FLUX measurement is taken at a given parallactic angle and enters into the final mean with its individual weight, it is necessary to subtract the effects of sources in the reference arcs on a point-by-point basis. In practice the LEAD, MAIN, and TRAIL measurements for each referenced measurement are adjusted by the values determined using the positions and ΔT_a from Table 6. Only those sources with significant 18.5 GHz detections were used. In Table 7, we list the unweighted mean corrections $\Delta T_{\rm fld}$ applied to the data points in the contaminated fields. The center beam corrections $\Delta T_{\rm on}$ and maximum reference arc corrections $\Delta T_{\rm ref}$ (for the parallactic angle where the source is closest to the center of the arc) are also given.

The corrected SZE results are shown in Table 8. The second column lists the source contributions $\Delta T_{5.5\,\rm m}$(src) computed using the actual data weighting in the cases of A2142 and A2256, and the 3 σ limit for A478 (source A478.1). The corrected values $\Delta T_{5.5\,\rm m}$(corr) are listed in the final column, with the correction values themselves added in quadrature as an uncertainty. For A478, the 1 σ limit on the contribution of source A478.1 was used as the uncertainty. The measurement of the SZE in the weakest cluster A2256 is most adversely affected by the correction uncertainties, with the statistical standard error increasing from 6.4% to 12%. The error bars on the A478 and A2142 are not as strongly affected owing to the larger relative decrements. However, in all three cases, the corrections applied were similar in magnitude to or larger than the purely statistical measurement uncertainties and thus contribute significantly to the error budgets. More accurate SZE measurements will require better source measurements, necessarily contemporaneous with the SZE observations to deal with possible variability in the foreground sources.

TABLE 7

TOTAL SOURCE CONTRIBUTIONS TO 5.5 METER SZE FIELDS

Field	$N_{\rm on}$	$\Delta T_{\rm on}$ (μK)	$N_{\rm ref}$	max $\Delta T_{\rm ref}$ (μK)	$\Delta T_{\rm fld}$ (μK)
A2142L.....	1	0.6	1	-23.7	-0.7
A2142	1	17.8	1	-4.8	16.2
A2142T.....	0	0.0	1	-2.0	-0.2
A2256	1	24.5	0	0.0	24.5

TABLE 8

FINAL SZE RESULTS

Cluster	$\Delta T_{5.5\,\rm m}$(obs) (μK)	$\Delta T_{5.5\,\rm m}$(src) (μK)	$\Delta T_{5.5\,\rm m}$(corr) (μK)
A478	-375 ± 24	<44	-375 ± 28 [a]
A2142.....	-420 ± 19	17	-437 ± 25
A2256.....	-218 ± 14	25	-243 ± 29

[a] A478 source limit 3 σ; used 1 σ for uncertainty.

6. THE SZE, BARYONIC MASS, AND H_0

The SZE is proportional to the Compton y-parameter

$$y = \int_{-\infty}^{\infty} \frac{kT_e}{m_e c^2}\, \sigma_T\, n_e\, d\zeta\ . \qquad (24)$$

For convenience, we will use cylindrical coordinates (R, ϕ, ζ) (R, ζ in Mpc) centered upon the cluster with ζ along the line of sight. Then

$$y(R, \phi) = \int_{-\infty}^{\infty} \frac{k\sigma_T}{m_e c^2} n_e(R, \phi, \zeta) T_e(R, \phi, \zeta) d\zeta \,. \quad (25)$$

For the small angles considered here, $R = D_a \theta$ for angular diameter distance D_a to the cluster. For $q_0 = \frac{1}{2}$ and $H_0 = 100\, h$ km s^{-1} Mpc^{-1}, which we will assume throughout this paper,[3]

$$D_a = 6000 \frac{(1+z) - \sqrt{1+z}}{(1+z)^2} h^{-1} \text{ Mpc} \,. \quad (26)$$

The on-sky intensity differences are measured in units of *antenna temperature* ΔT_a, which is the equivalent temperature difference in the Rayleigh-Jeans limit

$$\Delta I_\nu = \frac{2k\nu^2}{c^2} \Delta T_a \,. \quad (27)$$

Using the standard formulae for the fractional change in the intensity of the thermal background in the nonrelativistic limit (Sunyaev & Zeldovich 1980), we get the frequency dependence of the measured change in antenna temperature of the microwave background due to the SZE:

$$\frac{\Delta T_a}{T_{\rm cmb}} = y \frac{x^2 e^x}{(e^x - 1)^2} \left(x \coth \frac{x}{2} - 4 \right), \quad (28)$$

where x is the dimensionless frequency

$$x = \frac{h\nu}{kT_{\rm cmb}} = \frac{\nu}{56.80 \text{ GHz}} \,. \quad (29)$$

We use the COBE FIRAS value for the microwave background temperature $T_{\rm cmb} = 2.726 \pm 0.010$ K (Mather et al. 1994). At the 5.5 m observing frequency $\nu = 32$ GHz ($x = 0.563$) this is

$$\frac{\Delta T_a}{T_{\rm cmb}} = -1.897 y \,. \quad (30)$$

There are several possible corrections to the expressions (28) and hence (30). In addition to the thermal SZE, there is a kinematic effect due to the peculiar velocity of the cluster (Sunyaev & Zeldovich 1980). At 32 GHz, a peculiar velocity of 300 km s^{-1} for a cluster with $kT_e = 7.5$ keV will produce a change in the SZE intensity of only 2% and can safely be ignored in these calculations.

Another factor not accounted for in our expression for y is the relativistic correction to equation (28), which was derived in the nonrelativistic limit. Rephaeli (1995) has calculated the corrections for the low optical depths ($\tau < 10^{-2}$) and mildly relativistic electron temperatures ($kT_e \sim 5$–10 keV) appropriate to our clusters. For these parameters, Rephaeli finds corrections of around $+3\% \pm 0.3\%$ at our observing $x = 0.563$, i.e., the SZE decrement is less pronounced in magnitude than what equation (28) would predict. Because this is a systematic underestimation of y given an observed ΔT_a, we use the corrected relation

$$y_{\rm meas} = -\frac{\chi_{\rm rel} \Delta T_a}{1.897 T_{\rm cmb}} \,, \quad (31)$$

where the relativistic correction factors $\chi_{\rm rel}$ for each cluster are given in Table 10, along with the Compton parameters $y_{\rm meas}$ using the source-corrected ΔT_a from Table 8.

Herbig et al. (1995) carried out SZE observations and analysis of the Coma Cluster using the same 5.5 m setup and calibration scale as was employed in our observations. With source corrections and calibration uncertainty included, they found a nonrelativistic y-parameter of $y_{\rm meas} = (5.96 \pm 0.99) \times 10^{-5}$. If we apply the relativistic correction 1.029 to the Herbig et al. measurement and remove the 6.9% calibration uncertainty, we get $y_{\rm meas} = (6.13 \pm 0.93) \times 10^{-5}$. This is the value we have given in Table 10.

The observed SZE decrement is the true decrement modified by the telescope primary beam and the beam switching. The 5.5 m single-beam pattern is well approximated by a circular Gaussian

$$g(\theta) = \frac{1}{2\pi\theta_{\rm G}^2} \exp\left(-\frac{\theta^2}{2\theta_{\rm G}^2} \right) \quad (32)$$

with beam width $\theta_{\rm G} = 3\farcm12 \pm 0\farcm04$ ($7\farcm35 \pm 0\farcm10$ FWHM). The beam is less than 1.4% elliptical. Because clusters track through a range of parallactic angles, the slightly elliptical beam is rotated on-sky, and therefore the effective beam is well represented by the geometric mean $\theta_{\rm G}$.

The average Compton y-parameter in the Gaussian beam, on a line of sight offset at cylindrical radius R from the center at position angle ϕ, for small angles is given by

$$y_{\rm G}(R, \phi) = \int_0^{2\pi} d\theta \int_0^{\infty} r\, dr \frac{1}{2\pi L_{\rm G}^2} e^{-d^2/2L_{\rm G}^2} y(r, \phi - \theta) \,,$$
$$d^2 = R^2 + r^2 - 2Rr \cos(\theta) \,. \quad (33)$$

Here $L_{\rm G} = D_a \theta_{\rm G}$. The beam switching can be evaluated as

$$y_{\rm sw}(R, \phi; \psi_p) = y_{\rm G}(R, \phi) - \tfrac{1}{2} y_{\rm G}(R_-, \phi_-) - \tfrac{1}{2} y_{\rm G}(R_+, \phi_+) \quad (34)$$

with

$$R_\pm^2 = D^2 \sin^2(\psi_p + \phi) + [R \pm D \cos(\psi_p + \phi)]^2 \quad (35a)$$

$$\tan \phi_\pm = \frac{R \sin \phi \mp D \sin \psi_p}{R \cos \phi \pm D \cos \psi_p} \,. \quad (35b)$$

The 5.5 m beam separation is $\theta_D = 22\farcm16$, so $D = D_a \theta_D$, and ψ_p is the principal parallactic angle for the observation. For convenience, the position angle ϕ is measured starting from the east so it is in the same orientation as the parallactic angle ψ.

We will most often use the integrals through the cluster center in a cylindrically symmetric model. The angular dependences are dropped, so $y_{\rm G}(R, \phi) = y_{\rm G}(R)$ is now a function of angular radius from the cluster center only. The expressions (33) and (34) are abbreviated as

$$y_{\rm G} \equiv y_{\rm G}(0) = 2\pi \int_0^{\infty} r\, dr \frac{1}{2\pi L_{\rm G}^2} e^{-r^2/2L_{\rm G}^2} y(r) \quad (36)$$

and

$$y_{\rm sw} \equiv y_{\rm sw}(0) = y_{\rm G}(0) - y_{\rm G}(D) \,. \quad (37)$$

[3] At these low redshifts, the effect of the cosmology is purely kinematic and thus depends only upon q_0. To first order, $\Delta D_a / D_a \approx \Delta q_0 z/2$, which at our redshift limit of $z = 0.1$ makes a $\pm 2.5\%$ change in D_a, and thus the derived h, for $\Delta q_0 = \pm\frac{1}{2}$.

6.1. *Density Models for the ICM*

The distribution of the X-ray–emitting gas in galaxy clusters has frequently been modeled by an isothermal β-model (Cavaliere & Fusco-Femiano 1976), also known as a modified isothermal King model. In this spherically symmetric model, the electron gas density n_e is given as a function of the spherical radius r from the center of the cluster by

$$n_e = n_0\left(1 + \frac{r^2}{r_c^2}\right)^{-3\beta/2}, \tag{38}$$

where r_c is the core radius of the cluster and n_0 is the density at $r = 0$. For the present, we will consider mass distributions with circular symmetry in the plane of the sky, although it is easy to generalize to ellipsoidal profiles.

Table 9 lists published parameters of the intracluster gas from various X-ray observations of A478, A2142, A2256, and Coma. The core radius $\theta_{\rm core}$ determined from the X-ray surface brightness profile is listed and has been converted into a linear size r_c in h^{-1} Mpc using equation (26). The overall temperature of the X-ray–emitting gas T_e is given as kT_e in keV (10^8 K = 8.61 keV). As determined from the X-ray emission, the central densities n_0 are in units of $h^{1/2}$ cm^{-3}. A value for β is given only if it has been determined by fitting the surface brightness profile. All errors are given as 1 σ, converted from 90% confidence ($\approx$1.645 σ) in the literature if necessary.

We now discuss the models for each cluster in detail. Because the model uncertainties are in most cases the dominant source of systematic error in the determinations of the baryonic masses and Hubble constant for this sample, we plan to make our own detailed analysis of the *ROSAT* data for these clusters to obtain more accurate models and to understand the limitations of our particular method better. For now, we adopt the models presented in the literature and proceed with our analysis.

6.1.1. *A478*

Abell 478 has been shown to contain one of the largest cluster cooling flows with more than $5 \times 10^{11}\ h^{-1}\ M_\odot$ of X-ray absorbing matter within the inner 150 h^{-1} kpc and a total mass deposition rate of $\sim$500 $h^{-1}\ M_\odot$ yr^{-1} (Johnstone et al. 1992; Allen et al. 1993). The combined *Ginga* and *ROSAT* data measure the temperature $kT_e = 6.56 \pm 0.09$ keV for the cluster isothermal component and a temperature of $kT_e \sim 3$ keV within the inner 75 h^{-1} kpc. The *ROSAT* PSPC image of A478 (Allen et al. 1993) shows an axial ratio of $\sim$0.8 to the inner ($\theta < 2'.4$) isophotal contours. This would suggest that A478 is probably even more ellipsoidal than this and should be kept in mind in the following analysis.

The presence of such a large cooling component to the cluster core medium makes modeling of the SZE from the X-ray emission difficult. Edge & Stewart (1991) found $T_e = 6.8$ keV, $r_c = 0.10\ h^{-1}$ Mpc, and $n_0 = 25.2 \pm 2.8 \times 10^{-3}\ h^{1/2}$ cm^{-3} from *EXOSAT* observations. Allen et al. (1993) fitted a central electron density to the isothermal (noncooling) component of $n_0 \approx 9.55 \times 10^{-3}\ h^{1/2}$ cm^{-3} assuming a core radius of $r_c = 0.125\ h^{-1}$ Mpc and a King profile ($\beta = \frac{2}{3}$).

We have adopted the Allen et al. (1993) values for n_0, r_c, and β. The uncertainties on these quantities were determined empirically by comparison with our own preliminary analysis of the *ROSAT* data. This model is the one listed in Table 9.

6.1.2. *A2142*

A2142 is the most distant cluster ($z = 0.0899$) and has the largest 2–10 keV luminosity in our sample. A2142 is also the second most luminous cluster in the Edge sample as a whole. Edge & Stewart (1991) list A2142 as a cooling core cluster, and Edge, Stewart, & Fabian (1992) derive a mass flow rate of 50–150 $h^{-1}\ M_\odot$ yr^{-1}.

In the compilation of cluster temperatures by David et al. (1993), A2142 is listed as having a *Ginga* temperature of $kT_e = 8.68 \pm 0.12$ keV. Abramopolous & Ku (1983) derive $r_c = 0.26 \pm 0.01\ h^{-1}$Mpc and $n_0 = 6.97 \pm 0.41 \times 10^{-3}\ h^{1/2}$ cm^{-3}, where we have estimated the uncertainty in n_0 through the relation $n_0 \propto L_{\rm X}^{1/2} r_c^{-3/2}$. The parameter β is fixed at unity in this model. For want of a better determination, we adopt $\beta = 1 \pm 0.3$.

6.1.3. *A2256*

Although A2256 does not appear to have a central cooling flow (Edge et al. 1992), it does show significant substructure in the X-ray–emitting gas. Briel et al. (1991) found evidence for a "merger event" in the *ROSAT* PSPC image of the cluster. Two surface brightness peaks were found in the cluster center with a separation of 3'.5 (160 h^{-1} kpc), with some indication of differing temperatures. David et al. (1993) list an overall *Ginga* temperature $kT_e = 7.51 \pm 0.11$ keV, while the *ROSAT* PSPC data give $kT_e \sim 2.0$ keV for the cooler (northwest) subcluster. Fits of the azimuthally averaged data excluding the secondary maximum to a modified isothermal King profile yielded $\theta_{c,1} = 4'.83 \pm 0'.17$ and $\beta_1 = 0.756 \pm 0.013$, while a fit to the secondary after subtraction of the primary smooth profile gave $\theta_{c,2} = 4'.3 \pm 0'.4$ and $\beta_2 = 1.1 \pm 0.1$ and a peak surface brightness 82% of that of the primary. Briel et al. (1991) also analyze the distribution of 87 galaxies to find radial velocity dispersions of 1270 ± 127 km s^{-1} for the main cluster region and 250 ± 123 km s^{-1} in the northwest subcluster. A relative

TABLE 9

X-Ray Cluster Parameters

Cluster	z	$\theta_{\rm core}$ (arcmin)	kT_e (keV)	$n_0/10^{-3}$ ($h^{1/2}$ cm^{-3})	β	r_c (h^{-1} Mpc) [a]
A478	0.0881	1.93 ± 0.30	6.56 ± 0.09	9.55 ± 1.75	0.667 ± 0.029	0.128 ± 0.020
A2142.....	0.0899	3.69 ± 0.14	8.68 ± 0.12	6.97 ± 0.41	1.0 ± 0.3	0.249 ± 0.009
A2256.....	0.0581	5.33 ± 0.20	7.51 ± 0.11	3.55 ± 0.18	0.795 ± 0.020	0.245 ± 0.009
Coma	0.0235	10.50 ± 0.60	9.10 ± 0.40	4.09 ± 0.06	0.750 ± 0.030	0.207 ± 0.012

Note.—X-ray temperatures from *Ginga* (David et al. 1993), except Coma (Hughes et al. 1988). Other parameters A478 from Allen et al. 1993 and our own analysis of *ROSAT* data; A2142 from Abramopoulos & Ku 1983; A2256 from Henry et al. 1993; Coma r_c, n_0 and β from Briel et al. 1992.

[a] Assumes $q_0 = 1/2$.

systemic velocity difference of -2150 ± 259 km s^{-1} is found between the northwest region and the main cluster—this difference is consistent with the infall velocity at 1 Mpc from a 10^{15} $M_\odot$ cluster. The pointing center used in our observations is approximately in the center, between the two components of A2256.

Davis & Mushotzky (1993) examined *Einstein* IPC data and also found evidence for the merger, and they derive $\theta_c = 6'.0^{+0.9}_{-0.7}$ and $\beta = 0.72^{+0.10}_{-0.08}$. By fitting elliptical isophotes, we find axial ratios of 0.6 near the center to 0.25 at a radius of 10′. Spectroscopy from the *BBXRT* (Miyaji et al. 1993) indicates a temperature of $kT_e = 4.6^{+0.9}_{-0.7}$ keV for the northwest component.

A more detailed analysis of the A2256 *ROSAT* PSPC data has been carried out by Henry, Briel, & Nulsen (1993). From their data, an isothermal model of the intracluster medium has been derived: $\theta_c = 5'.33 \pm 0'.20$, $\beta = 0.795 \pm 0.020$, $n_0 = 3.55 \pm 0.18 \times 10^{-3}$ $h^{1/2}$ cm^{-3}. They derived a low-energy temperature from the *ROSAT* data of $kT_e = 6.9 \pm 0.6$ keV, which is consistent with the *Ginga* temperature. We choose to adopt the Henry et al. parameters and the David et al. *Ginga* temperature.

6.1.4. *Coma*

The Coma Cluster is also a member of our sample. Briel, Henry, & Böhringer (1992) present an isothermal X-ray model for the Coma gas with $\beta = 0.75 \pm 0.03$ and $\theta_c = 10'.5 \pm 0'.6$ ($r_c = 0.207 \pm 0.012$ h^{-1} Mpc for an assumed redshift of $z = 0.0235$). They adopt an electron temperature of $kT_{\rm eff} = 8.2 \pm 0.2$ keV, obtained from *Ginga* measurements.

Earlier observations by Hughes, Gorenstein, & Fabricant (1988) with *EXOSAT* give a slightly higher temperature of $kT_{\rm eff} = 8.5 \pm 0.3$ keV. After deprojection and subtraction of Galactic absorption, they fitted a model with $\beta = 0.63 \pm 0.03$ and $\theta_c = 7'.6 \pm 0'.4$, and central electron density of $n_0 \approx 3 \times 10^{-3}$ $h^{1/2}$ cm^{-3}. For a best-fit model using the *EXOSAT* and *Tenma* data, they assume an isothermal core with the high temperature of $kT_{\rm iso} = 9.1 \pm 0.4$ keV, which extends out to a radius of $\theta_{\rm iso} = 23' \, {}^{-8'}_{+12'}$, beyond which the temperature falls almost adiabatically (polytropic index $\gamma \sim 1.555$). This gives a temperature profile outside the isothermal radius $R_{\rm iso}$ of

$$T(R) = T_{\rm iso}\left[\frac{1 + (R/r_c)^2}{1 + (R_{\rm iso}/r_c)^2}\right]^{-(3\beta/2)(\gamma-1)} \qquad R > R_{\rm iso} \, . \quad (39)$$

This is the model adopted by Herbig et al. (1995), although with n_0, r_c, and β as given by Briel, Henry, & Böhringer.

The higher temperature may in fact be indicated by *ASCA* observations of Coma (see Fabian et al. 1994), which prefer temperatures of $kT_{\rm eff} \sim 9$ keV. For consistency with Herbig et al., we adopt the Briel, Henry, & Böhringer n_0, r_c, and β and a temperature $kT_{\rm eff} = 9.1 \pm 0.4$ keV. In the model calculations in this paper, we do not include an isothermal cutoff, and this makes only a few percent difference.

6.1.5. *Model-dependent Quantities*

Using the isothermal β-model with electron temperature T_e, the y at a point at projected radius $t = R/r_c$ from the cluster center (eq. [24]) has the familiar form

$$y(t) = \frac{kT_e}{m_e c^2} n_0 \sigma_T r_c \int_{-\infty}^{\infty} ds (1 + t^2 + s^2)^{-(3\beta/2)} = y_0 (1 + t^2)^{(1/2)-(3\beta/2)} \, , \quad (40)$$

TABLE 10

EFFICIENCIES AND RELATIVISTIC CORRECTIONS

Cluster	$\eta_{\rm G}$	$\eta_{\rm obs}$	$\chi_{\rm rel}$	$y_{\rm meas}$ (10^{-5})
A478	0.826 ± 0.028	0.414 ± 0.008	1.022	7.41 ± 0.55
A2142.....	0.947 ± 0.081	0.498 ± 0.090	1.030	8.70 ± 0.50
A2256.....	0.818 ± 0.014	0.612 ± 0.003	1.026	4.82 ± 0.58
Coma	0.618 ± 0.026	0.563 ± 0.021	1.029	6.13 ± 0.93

where y_0 is the y-parameter at zero projected radius

$$y_0 = 7.12 \times 10^{-5} \, h^{-1/2} \frac{\Gamma[(3\beta - 1)/2]}{\Gamma(3\beta/2)} \times \left(\frac{n_0}{10^{-3} \, h^{1/2} \, {\rm cm}^{-3}}\right)\left(\frac{T_e}{10 \, {\rm keV}}\right)\left(\frac{r_c}{h^{-1} \, {\rm Mpc}}\right) . \quad (41)$$

The dependence on h is due to the choice of the units for n_0 and r_c, which in turn are determined from the X-ray measurements. The resulting factor of $h^{1/2}$ will be used to determine the value of the Hubble constant by comparison with the observed y-parameters.

Given the model for the density profile $n_e(R, \phi, \zeta)$ in the cluster, we can determine the efficiency $\eta_{\rm obs}$ at which our switched observations can recover the SZE that an ideal pencil beam through the cluster center would measure

$$\eta_{\rm obs} = \frac{y_{\rm sw}}{y_0} \, . \quad (42)$$

In addition, we can compute the efficiency $\eta_{\rm G}$ at which the SZE is measured with respect to an ideal Gaussian main beam

$$\eta_{\rm G} = \frac{y_{\rm sw}}{y_{\rm G}} \, . \quad (43)$$

These efficiencies depend upon the model only through θ_c and β. The derived efficiencies (for a pointing center at the cluster center $R = 0$) for the OVRO 5.5 m SZE observations are given in Table 10. The uncertainties in the $\eta_{\rm obs}$ and $\eta_{\rm G}$ were determined numerically using the stated uncertainties in the model θ_c and β.

Other model-derived quantities of interest are the equivalent spherical volume

$$V_s(R) = 4\pi r_c^3 \int_0^{R/r_c} dt t^2 (1 + t^2)^{-3\beta/2} \quad (44)$$

and the Gaussian cylindrical volume

$$V_{\rm G}(L_{\rm G}) = 2\pi r_c^3 \frac{\Gamma(1/2)\Gamma[(3\beta - 1)/2]}{\Gamma(3\beta/2)} \times \int_0^{\infty} dt \, t \exp\left(-\frac{r_c^2 t^2}{2L_{\rm G}^2}\right)(1 + t^2)^{(1/2)-(3\beta/2)} \, . \quad (45)$$

These quantities are the equivalent volumes for a uniform density cluster at the central density n_0.[4] These volumes are important for relating the observed X-ray emission and the

[4] Note that eqs. (44) and (45) can respectively be written in terms of the incomplete beta function and the incomplete gamma function. However, it is easiest to evaluate these integrals numerically, using Maple or Mathematica, for example.

observed SZE to the implied baryonic mass contained within the cluster.

6.2. *Baryonic Mass in Clusters*

Given knowledge about the electron temperature in the intracluster gas, we can use the y-parameter to measure a baryonic mass M_b for the ionized phase. For a general density model,

$$M_b = \iiint dR\, d\phi\, d\zeta \alpha' m_b n_e(R, \phi, \zeta) . \quad (46)$$

Comparison with equation (24) gives for our cylindrical model

$$M_b = \frac{m_e c^2}{\sigma_T k T_{\rm eff}} \alpha' m_b 2\pi \int dR y(R) , \quad (47)$$

where α' is the number of baryons per electron, and m_b is the baryon (nucleon) mass. Considering only H and He at 12:1 in number of atoms, $\alpha' \approx 8/7$. For a general temperature distribution, the effective temperature is given by

$$T_{\rm eff} = \frac{\iiint dR\, d\phi\, d\zeta n_e(R, \phi, \zeta) T_e(R, \phi, \zeta)}{\iiint dR\, d\phi\, d\zeta n_e(R, \phi, \zeta)} , \quad (48)$$

which reduces to the single temperature $T_{\rm eff} = T_e$ for an isothermal cluster medium at electron temperature T_e.

By combining equation (47) with equation (36), we can determine the temperature-weighted baryonic mass within the cylinder defined by the 7.′35 FWHM Gaussian beam of the 5.5 m telescope through the cluster center

$$M_{\rm G} = \alpha' m_b n_0 V_{\rm G} = \frac{m_e c^2}{\sigma_T k T_{\rm eff}} 2\pi L_{\rm G}^2 \alpha' m_b y_{\rm G} , \quad (49)$$

where $L_{\rm G} = D_a \theta_{\rm G}$ as before. Hence, the baryonic mass may be written as

$$M_{\rm G} = 4.407 \times 10^{14} \left(\frac{1 \text{ keV}}{T_{\rm eff}}\right) \left(\frac{L_{\rm G}}{h^{-1} \text{ Mpc}}\right)^2 \times \left(\frac{y_{\rm sw}}{10^{-5} \eta_{\rm G}}\right) h^{-2} M_\odot . \quad (50)$$

The efficiency factor $\eta_{\rm G} = y_{\rm sw}/y_{\rm G}$ converts the measured $y_{\rm sw}$ into the $y_{\rm G}$ within the Gaussian main beam. A better representation of the SZE in terms of a mass is the surface baryonic mass density within the Gaussian cylinder

$$\Sigma_{\rm G} = \frac{M_{\rm G}}{2\pi L_{\rm G}^2} = 7.013 \times 10^{13} \left(\frac{1 \text{ keV}}{T_{\rm eff}}\right) \times \left(\frac{y_{\rm sw}}{10^{-5} \eta_{\rm G}}\right) M_\odot \text{ Mpc}^{-2} . \quad (51)$$

The surface density is distance independent and is a more consistent parameter than the mass, which will vary with the resolution $L_{\rm G}$. The values to use for $y_{\rm sw}$ are the measured y-parameters $y_{\rm meas}$, with relativistic corrections applied using equation (31), found in Table 10. The derived baryonic masses for our clusters are given in Table 11. The clusters have similar surface densities $\Sigma_{\rm G} \sim 7 \times 10^{13} M_\odot$ Mpc^{-2}.

The factor $\eta_{\rm G}$ and the effective temperature $T_{\rm eff}$ are the only model-dependent quantities in $M_{\rm G}$ and $\Sigma_{\rm G}$. In Table 11, we use the X-ray model parameters listed in Table 9. Since equations (50) and (51) are linear in the observable $y_{\rm sw}$, the SZE is potentially a more accurate probe of the baryonic mass than the X-ray emission.

TABLE 11

BARYONIC MASSES FROM THE SZE

Cluster	$L_{\rm G}$ (h^{-1} Mpc) [a]	$\Sigma_{\rm G}$ (10^{13} $M_\odot$ Mpc^{-2})	$M_{\rm G}$ ($10^{13} h^{-2}$ $M_\odot$)
A478	0.207	9.59 ± 0.79	2.58 ± 0.21
A2142.....	0.211	7.42 ± 0.77	2.08 ± 0.22
A2256.....	0.143	5.50 ± 0.67	0.71 ± 0.09
Coma	0.0615	7.64 ± 1.25	0.18 ± 0.03

[a] Assumes $q_0 = \frac{1}{2}$.

The X-ray emission from clusters has been used to determine the baryonic mass fraction by comparison with derived total masses. This calculation has been done for Coma (White et al. 1993) and A2256 (Henry et al. 1993). The SZE is an independent measure of the mass within the Gaussian cylinder of the beam. We can use the X-ray–derived model to relate $M_{\rm G}$ to the mass within the sphere

$$M_{\rm SZE}(R) = M_{\rm G} \frac{V_s(R)}{V_{\rm G}} , \quad (52)$$

where $V_{\rm G}$ is the Gaussian volume (eq. [45]) within the beam on the cluster.

For our clusters A478, A2142, and A2256, as well as Coma, the baryonic masses are given in Table 11. In Table 12, gravitational masses have been obtained from the literature, and the baryonic fraction within some given fiducial radius R_0 is computed. The model-dependent factors $V_s/V_{\rm G}$ are listed for the assumed R_0, along with the 1 σ uncertainties computed from the model uncertainties in r_c and β.

White & Fabian (1995) discuss the "baryon overdensity" problem in the context of *Einstein* observations of a number of clusters, including A478 and A2142. Henry et al. (1993) give detailed models and masses for A2256, and White et al. (1993) compute the enclosed baryonic and gravitational masses for Coma. We discuss the results for each cluster, and the four clusters as a group, below.

6.2.1. *A478*

White & Fabian (1995) consider a radius of $R_0 = 0.976$ h^{-1} Mpc within which they find an X-ray–determined gas fraction $M_{\rm Xray}/M_{\rm tot} = 0.091 \pm 0.008\, h^{-3/2}$. No uncertainties in the values for $M_{\rm tot}$ are stated, although they are likely to be high (probably 20% or more). This should be kept in mind when evaluating the uncertainties for the clusters listed in the White & Fabian paper.

For the model in Table 9, our SZE measurements give a Gaussian mass of $M_{\rm G} = (2.58 \pm 0.21) \times 10^{13}$ h^{-1} $M_\odot$ within the 5 m beam. This model gives a ratio $V_s/V_{\rm G} = 2.99 \pm 0.08$ within $R_0 = 0.976$ h^{-1}Mpc, so we find an SZE-indicated baryonic mass of $M_{\rm SZE} = (7.71 \pm 0.66) \times 10^{13}$ h^{-2} $M_\odot$. Using the gravitational mass from White & Fabian, we get a baryonic fraction of $M_{\rm SZE}/M_{\rm tot} = 0.166 \pm 0.014\, h^{-1}$.

The cluster A478 stands out with a higher baryonic fraction from both the X-ray and SZE measurements and has a stronger SZE decrement than expected from the X-ray measurements (giving a lower implied Hubble constant from the ratio $M_{\rm Xray}/M_{\rm SZE}$), when compared with the other clusters in this sample (see below, and in the next section). These

TABLE 12

BARYONIC FRACTIONS IN THE CLUSTERS

Cluster	R_0 (h^{-1} Mpc)	$V_s(R_0)/V_G$	M_{sze} ($10^{13}\ h^{-2}\ M_\odot$)	M_{tot} ($10^{13}\ h^{-2}\ M_\odot$)	M_{sze}/M_{tot} (h^{-1})
A478 [a]	0.976	2.99 ± 0.08	7.7 ± 0.7	46.4	0.166 ± 0.014
A2142 [a]	0.966	2.90 ± 0.43	6.0 ± 1.1	100.5	0.060 ± 0.011
A2256 [b]	0.76	4.29 ± 0.05	3.0 ± 0.4	51 ± 14	0.060 ± 0.018
Coma [c]	1.50	38.3 ± 3.0	6.9 ± 1.3	110 ± 22	0.063 ± 0.017

[a] A478 and A2142 M_{tot} from White & Fabian 1995. No uncertainties given.
[b] A2256 M_{tot} from Henry, Briel, & Nulsen 1993.
[c] Coma M_{tot} from White et al. 1993.

discrepancies may be explained by elongation of the cluster along the line of sight, as indicated by its observed ellipticity in the plane of the sky. We will discuss this further in the context of the Hubble constant in the next section.

6.2.2. *A2142*

For A2142, White & Fabian (1995) find an X-ray–determined gas mass fraction $M_{Xray}/M_{tot} = 0.050 \pm 0.003\ h^{-3/2}$ within $R_0 = 0.976\ h^{-1}$ Mpc. Our SZE measurements give a Gaussian mass of $M_G = (2.08 \pm 0.22) \times 10^{13}\ h^{-1}\ M_\odot$ with an efficiency of $V_s/V_G = 2.90 \pm 0.43$ for $R_0 = 0.976\ h^{-1}$ Mpc. Therefore, $M_{SZE} = (6.03 \pm 1.10) \times 10^{13}\ h^{-2}\ M_\odot$ and $M_{SZE}/M_{tot} = 0.060 \pm 0.011\ h^{-1}$.

6.2.3. *A2256*

Henry et al. (1993) fit a model with $r_c = 0.245 \pm 0.009\ h^{-1}$ Mpc, compared to the 5 m beam size of $L_G = 0.143\ h^{-1}$ Mpc at redshift $z = 0.0581$. They derive an enclosed mass of $M_{tot} = (5.1 \pm 1.4) \times 10^{14}\ h^{-1}\ M_\odot$ within $R_0 = 0.76\ h^{-1}$ Mpc. From the X-ray data they find $M_{Xray}/M_{tot} = 0.063 \pm 0.039\ h^{-3/2}$. Assuming our isothermal model, we find a ratio $V_s/V_G = 4.29 \pm 0.05$ within the sphere of radius R_0. The SZE measurements gave a Gaussian mass of $M_G = (7.1 \pm 0.9) \times 10^{12}\ h^{-1}\ M_\odot$ within the 5 m beam; thus, $M_{SZE} = (3.05 \pm 0.39) \times 10^{13}\ h^{-2}\ M_\odot$ in the sphere, and $M_{SZE}/M_{tot} = 0.060 \pm 0.018\ h^{-1}$.

6.2.4. *Coma*

For Coma, White et al. (1993) adopt a (model-dependent) total mass of $M_{tot} = (1.10 \pm 0.22) \times 10^{15}\ h^{-1}\ M_\odot$ within a sphere of radius $R_0 = 1.5\ h^{-1}$ Mpc (the Abell radius). They find $M_{Xray}/M_{tot} = 0.050 \pm 0.013\ h^{-3/2}$. Our adopted isothermal model with an assumed temperature of $kT_{eff} = 9.10.4$ keV gives the Gaussian mass of $M_G = (1.81 \pm 0.30) \times 10^{12}\ h^{-1}\ M_\odot$ within the 5 m beam. For a spherical radius of $R_0 = 1.5\ h^{-1}$ Mpc, the ratio $V_s/V_G = 38.3 \pm 3.0$, and thus $M_{SZE} = (6.93 \pm 1.27) \times 10^{13}\ h^{-2}\ M_\odot$. Using this value, we find $M_{SZE}/M_{tot} = 0.063 \pm 0.017\ h^{-1}$, in agreement with the White et al. fraction for $h = 0.62^{+0.36}_{-0.28}$.

For the Coma Cluster, the 7.35 5 m beam is small ($L_G = 61.5\ h^{-1}$ kpc) compared to the Abell radius $R_0 = 1.5\ h^{-1}$ Mpc, and we are making a large Gaussian correction $V_s/V_G \sim 38$. In addition, the contribution of the SZE signal in the reference beams is significant, so the details of the electron temperature profile in these outer parts are more important than in the other clusters.

6.2.5. *The Sample*

We see that in three of the four clusters (A2142, A2256, and Coma) the SZE-determined baryonic fractions M_{SZE}/M_{tot} are consistent, with a mean of $0.061 \pm 0.010\ h^{-1}$ (the uncertainty from the individual error bars, not the scatter). We exclude A478 from this average owing to the discrepancies between this cluster and the others in the sample (if A478 is included, the mean becomes $0.087 \pm 0.030\ h^{-1}$). We should also include the 6.9% calibration uncertainty, giving $\langle M_{SZE}/M_{tot} \rangle = 0.061 \pm 0.011\ h^{-1}$.

Strictly speaking, this is a *lower limit* on the baryon fraction M_B/M_{tot}, since we have not included the luminous mass in galaxies, and some of the dark matter may be baryonic. White et al. (1993) find a ratio $M_{gal}/M_{tot} = 0.009 \pm 0.003$ in Coma, compared to the fraction $M_{Xray}/M_{tot} = 0.050 \pm 0.013\ h^{-3/2}$ in hot gas. Henry et al. (1993) find similar relative fractions in galaxies and gas for A2256. Thus, we can safely assume that the luminous galaxies contribute around 20% or less of that mass contributed by the hot IGM. If we use the Coma value, and apply it to the sample as a whole, then $\langle M_B/M_{tot} = 0.009 \pm 0.003 + 0.061 \pm 0.011\ h^{-1}$. Note that for the low values of h, which are generally preferred, the contribution from luminous galaxies is further reduced relative to the gas. In this paper, we will use the SZE mass as a lower limit on the total baryon mass.

Standard estimates of the fraction of closure density in baryons for homogeneous big bang nucleosynthesis give $0.011 \leq \Omega_B h^2 \leq 0.015$ ($2\ \sigma$) (Smith et al. 1993). However, recent measurements of the deuterium abundance in the Lyman-α forest clouds in several QSOs lead to incompatible values for Ω_B that lie outside this range. One group finds a low value for the deuterium abundance (Tytler, Fan, & Burles 1996), which implies a high $\Omega_B h^2 = 0.024 \pm 0.006$, while the other finds a high deuterium abundance (Rugers & Hogan 1996), which implies a low $\Omega_B h^2 = 0.0062 \pm 0.0008$.

We can now estimate the total mass density parameter

$$\Omega_0 = \frac{\Omega_B}{M_B/M_{tot}} \leq \frac{\Omega_B}{M_{SZE}/M_{tot}}, \tag{53}$$

assuming that the baryonic fraction in clusters reflects that of the universe as a whole. Using our reduced sample average $\langle M_{SZE}/M_{tot} \rangle = 0.061 \pm 0.011\ h^{-1}$, and assuming standard nucleosynthesis limits $\Omega_B h^2 = 0.013 \pm 0.002$, one obtains $\Omega_0 h \leq 0.21 \pm 0.05$ (and $\Omega_0 h \leq 0.15 \pm 0.06$ if A478 is included in the mean). However, if one adopts the higher $\Omega_B h^2 = 0.024 \pm 0.006$, then our data imply a significantly higher limit $\Omega_0 h \leq 0.39 \pm 0.12$. On the other hand, if we use the high deuterium value giving a low $\Omega_B h^2 = 0.0062 \pm 0.0008$, then we find a low-density parameter $\Omega_0 h \leq 0.10 \pm 0.02$.

Using the standard nucleosynthesis values for Ω_B, we find the cluster data are consistent with $\Omega_0 = 1$ only for very low values of the Hubble constant ($h \approx 0.21$), or for similar values of baryonic mass segregation ($\Omega_{B,tot}/\Omega_{B,clus} \approx 0.21$).

Neither of these is indicated by other cosmological data. Extremely low values of h are not consistent with the estimates derived by comparison with the X-ray emission except in the case of A478 (see below). On the other hand, this result is consistent with large-scale structure studies that yield values in the range $0.2 \lesssim \Omega_0 h \lesssim 0.3$ (Efstathiou, Sutherland, & Maddox 1990; Efstathiou, Bond, & White 1992; Peacock & Dodds 1994). This widespread "baryon overdensity" problem has been seen in many clusters (see, e.g., White & Fabian 1995).

However, if the higher Ω_B from a low deuterium abundance is correct, then the values of the Hubble constant implied by comparison with the X-ray data (see below) would allow a critical density for the universe. Conversely, adoption of the high deuterium, low baryon density Ω_B would only exacerbate the baryon overdensity problem, which would force us to accept a low-density universe.

Departures from isothermality or the coexistence of multiple phases in the intracluster medium will introduce errors in our determination, as will model errors in the extrapolation to the spherical masses. In particular, the determined values for the total binding masses are uncertain. Measurements of total mass surface density from weak gravitational lensing would be particularly well suited to this method, as the angular size of a typical CCD frame is similar to that of the 5.5 m telescope beam width.

Note that our SZE (and X-ray) measurements count only the baryons in the hot IGM. The luminous baryonic matter in galaxies, and any nonluminous baryonic matter (such as in brown dwarfs, Jupiters, or compact objects), would be in addition to this estimate. Thus, we place a *lower limit* on the total baryonic mass and therefore on the baryonic fraction. The baryon overdensity problem would only get worse if there were substantial contributions from these other baryon reservoirs.

The difference between the SZE-based and X-ray–based estimates of the baryonic fraction is due to the different dependences on the Hubble constant, h^{-1} versus $h^{-3/2}$, respectively. If we compare the X-ray and SZE numbers given above for A2142, A2256, and Coma (thereby excluding A478), the average ratio is $\langle M_{\rm Xray}/M_{\rm SZE}\rangle = 0.889 \pm 0.099\, h^{-1/2}$ and therefore in agreement for $h = 0.79^{+0.19}_{-0.17}$. We explore this in more detail in the next subsection.

6.3. *The Hubble Constant*

The key to the determination of H_0 lies in the observation that the X-ray brightness and SZE decrement scale differently with temperature and density. Because the core radius r_c is determined from the observed angular size of the cluster ($r_c \propto h^{-1}$), the central densities of the cluster gas determined from X-ray data are proportional to $h^{1/2}$. The angular diameter–distance relation introduces a factor of h^{-1} into the y-parameter for the dependence on r_c (see eq. [41]). Thus, $y_{\rm pred}$, the estimate of the switched measurements of the Compton $y_{\rm sw}$ derived from the X-ray model in Table 9 using equations (37) and (36), are proportional to $h^{-1/2}$, and the observations of the actual SZE $y_{\rm meas}$ can therefore be used to find H_0:

$$h = \left(\frac{y_{\rm pred}}{y_{\rm meas}}\right)^2 . \tag{54}$$

The SZE model predictions $y_{\rm pred}$, the measured $y_{\rm meas}$, and the inferred Hubble constant values are given in Table 13. The uncertainties in $y_{\rm pred}$ were computed from the model parameter uncertainties. These parameters were assumed to vary independently, though in fact they are correlated from the X-ray–fitting procedure (particularly θ_c and β). A more direct approach, comparing the X-ray data and SZE data directly, as in Birkinshaw et al. (1991) and Birkinshaw & Hughes (1994), would be preferable. As it is, using the available information, the uncertainties quoted here are likely to be slightly inflated, as the parameter correlations will reduce the overall uncertainty somewhat. The asymmetrical 1 σ error bars on h are computed from the symmetrical 1 σ uncertainties on $h^{1/2}$.

In the discussions below, it is clear that when a detailed examination of nearby clusters is made, significant departures from the spherically symmetric, smooth, isothermal cluster "ideal" are seen. Improved X-ray models from *ASCA* and *ROSAT* are critical to the use of the SZE to determine H_0.

6.3.1. *A478*

Using this X-ray model based upon the Allen et al. (1993) *ROSAT* observations and the *Ginga* temperature, we derive a Hubble parameter $h^{1/2} = 0.57 \pm 0.14$ or $h = 0.32^{+0.18}_{-0.14}$. The largest contribution to the uncertainty comes from $y_{\rm pred}$ ($\pm 24\%$) rather than the 5.5 m telescope measurement $y_{\rm meas}$ ($\pm 7\%$). Thus, the largest improvement to be made is in the X-ray model.

The low value of $h = 0.32$ is similar to the value we obtained when calculating the baryonic masses and mass fractions in the previous section. A478 appears to have a much stronger SZE decrement than one would expect from the X-ray model, as well as a higher X-ray luminosity than one would expect from the size and velocity dispersion. One possible explanation for this is that A478 is significantly elongated along the line of sight, by around a factor of 2 compared with its dimensions in the plane of the sky. This would bring the implied value of the Hubble constant in line with the other clusters. It may also be that A478 is contaminated by the cooling flow emission. However, we have done some preliminary tests using a two-component model incorporating a low-temperature high-density phase, which gives nearly the same predicted SZE decrement, thus nearly the same Hubble constant. This cluster remains a puzzle and merits more detailed examination.

6.3.2. *A2142*

The X-ray model predictions and observed SZE give $h^{1/2} = 0.69 \pm 0.26$, or $h = 0.48^{+0.43}_{-0.29}$. The statistical error is dominated by the uncertainty in $y_{\rm pred}$ ($\pm 43\%$) rather than in $y_{\rm meas}$ ($\pm 6\%$). The largest single uncertainty is in the value of β. It will be important to improve the model with a detailed analysis of the *ROSAT* data.

6.3.3. *A2256*

Using the Henry et al. parameters and the *Ginga* temperature, combined with the 5.5 m telescope measurements of the SZE, we derive $h^{1/2} = 0.85 \pm 0.12$, and thus $h = 0.72^{+0.22}_{-0.19}$. The contributions to the error bar are $\pm 7\%$ from $y_{\rm pred}$ and $\pm 12\%$ from $y_{\rm meas}$. For this cluster, the dominant uncertainty is from the SZE measurement. It will be difficult to improve these measurements significantly, as it already has over 300 hr of integration time devoted to it. In addition, the CMB anisotropies on these scales are expected to

TABLE 13

HUBBLE CONSTANT FROM THE SZE

Cluster	y_{meas} (10^{-5})	y_{pred} (10^{-5} $h^{-1/2}$)	$h^{1/2}$	H_0 (km s^{-1} Mpc^{-1})
A478	7.4 ± 0.6	4.2 ± 1.0	0.57 ± 0.14	32^{+18}_{-14}
A2142.....	8.7 ± 0.5	6.0 ± 2.2	0.69 ± 0.26	48^{+43}_{-29}
A2256.....	4.8 ± 0.6	4.1 ± 0.3	0.85 ± 0.12	72^{+22}_{-19}
Coma	6.1 ± 0.9	...	0.82 ± 0.15	67^{+26}_{-22}
Sample.....	...	...	0.73 ± 0.08	54^{+12}_{-11}

be in the range 14–54 μK rms (see § 4). Clusters with SZE decrements weaker than that in A2256 will be very difficult to use for determination of the Hubble constant.

This cluster appears to have the best model, and cleanest X-ray and SZE data, though it is weaker than the others. Some possible problems not apparent in this analysis may be caused by the presence of the merging subclusters in the core, and the probable presence of very high temperature gas indicated by preliminary reports from *ASCA* (J. P. Henry, private communication). This should be kept in mind when evaluating the A2256 data (and similarly for the other clusters), and in the not too distant future *ASCA* and *ROSAT* should be able to provide much better constraints on the cluster models.

6.3.4. *Coma*

We will adopt the Herbig et al. determination of the Hubble constant, rather than use our own isothermal model (see Table 9). Because the Coma Cluster subtends a large angle on the sky compared with the switching angle, there is significant contribution of the SZ decrement to the reference beams, and thus the details of where the isothermal cluster atmosphere cuts off makes a noticeable difference to the derived Hubble constant.

Herbig et al. find a value of $h^{1/2} = 0.843 \pm 0.163$, which, after application of the relativistic correction ($\chi_{rel} = 1.029$) and removal of the 6.9% calibration uncertainty, becomes $h^{1/2} = 0.819 \pm 0.148$. This gives us $h = 0.67^{+0.26}_{-0.22}$. Note that adoption of a lower temperature, such as the Briel et al. value, will reduce the derived Hubble constant for Coma.

6.3.5. *Results for the Sample*

If the clusters in our sample are significantly ellipsoidal in shape, a value for H_0 can be obtained only by averaging a number of results from the unbiased sample. We combine the measurements for A478, A2142, A2256, and Coma (using our relativistically corrected Herbig et al. value), and the average is listed in Table 13. The most natural variable to average is $h^{1/2} = y_{pred}/y_{meas}$, for which the measurement and model errors should enter, as nearly as possible, in a Gaussian fashion, and for which projection effects (see below) should average out in an orientation unbiased sample. In this case, we get the mean $h^{1/2} = 0.733 \pm 0.076$, or $H_0 = 54^{+12}_{-11}$ km s^{-1} Mpc^{-1}. Note that the reduced $\chi^2 = 0.90$ on the 3 degrees of freedom against the mean $h^{1/2}$, so the spread in H_0 is consistent with the (large) error bars.

Up until this point, we have dealt with the "statistical" uncertainties introduced by the observations, calibration, and models. We should therefore now include the overall systematic calibration uncertainty of 6.9% (see § 3.3). Because all of the observations were calibrated using the same scale (including Coma), any error is correlated between the four cluster measurements and should thus be applied to the sample mean as a whole. Adding this uncertainty in quadrature, we find a sample average $h^{1/2} = 0.733 \pm 0.091$, or $H_0 = 54^{+14}_{-13}$ km s^{-1}Mpc^{-1}. This is the value that we adopt. The reader is reminded also that if the individual cluster measurements are to be used from Table 11 or from Table 13, then the 6.9% calibration uncertainty should be added to the statistical error bars listed there.

Because H_0 depends upon the *squares* of the ΔT of the model and of the measurement, the fractional errors in each are effectively doubled before adding in quadrature to make up the error budget in the Hubble constant. Accurate determination of H_0 therefore relies both upon accurate measurements of the SZE and upon an accurate model of the state of the intracluster medium (see discussion in Birkinshaw et al. 1991, and Inagaki, Suginohara, & Suto 1995).

At the beginning of this section, we discussed the systematic errors introduced by the relativistic corrections to the SZE, and the effect of a cluster peculiar velocity. In the former case, corrections to the y-parameter were made, and in the latter case, the corrections were dismissed as unlikely to be important.

The most serious potential source of systematic error in the determination of y_{pred} given the X-ray measurement is elongation of the cluster. Our analysis assumes that the line-of-sight extent of the cluster is the same as that in the plane of the sky. We have also assumed a spherical density profile in our analysis, though we would get the same result for an ellipsoidal cluster with r_c as the geometric mean core radius.

Deviations from circular symmetry in isophotes are not unusual: McMillan et al. (1988) studied 49 clusters observed by the *Einstein* satellite and found that the X-ray images had ellipticities of up to 0.5. As discussed in § 6.1, the X-ray isophotes of A478 and A2256 show evidence for significant ellipticity. Elliptical isophotes on the sky imply, at least statistically, a nonunity axial ratio in the line-of-sight dimension also.

There is some indication that the cluster A478, with its high implied baryonic mass fraction and low implied Hubble constant, may be an example of a highly elongated cluster. If A478 were excluded from our sample average, then we would find $h^{1/2} = 0.788 \pm 0.082$, or $H_0 = 62^{+14}_{-12}$ km s^{-1} Mpc^{-1}. However, without any clear indication of a problem with A478 given the large error bars, we choose to adopt the entire sample average.

It has been found that many clusters have significant cooling cores, and simple β-models may be inadequate to describe the state of the gas in these cases. Edge & Stewart (1991) list A478 and A2142 as cooling flow clusters. Cooling flow clusters are characterized by cores with gas at a significantly higher density and lower temperature than the surrounding gas. This causes a pronounced central peak in the X-ray surface brightness of the clusters. The cooling cores typically have radii of 50–200 kpc and temperatures reduced by up to a factor of 4 compared to the overall temperatures. Because the SZ decrement is more sensitive to the outer, low-density regions of the gas distribution than is the X-ray flux, central densities calculated from $S_X(r)$ at relatively large radii (Abramopoulos & Ku 1983; Jones & Forman 1984) should be used when possible. These densities are typically 2–3 times lower than the cooling core

densities found by Edge & Stewart (1991). Given X-ray images with high resolution and sensitivity, a better method would be to model n_e and T_e at large and small radii separately. Better models for the gas distribution are needed to account for the presence of cooling flows or other departures from a single spherically symmetric smooth isothermal profile.

7. CONCLUDING REMARKS

In summary, we find significant detections of the SZE for the clusters A478, A2142, and A2256 using the 5.5 m telescope at OVRO. These are the first observations to detect the effect in these clusters, although A478 and A2142 have been searched before (Lake & Partridge 1980; Birkinshaw,m Gull, & Northover 1981; Birkinshaw & Gull 1984; Chase et al. 1987). Observations of contaminating radio sources were carried out on the OVRO 40 m telescope. When the SZE measurements of the X-ray flux-limited sample are complete, an orientation-unbiased sample of clusters will be available for measurement of the Hubble constant.

The SZE is a measure of the electron pressure in the ionized cluster medium—with knowledge of the electron temperature, the SZE is proportional to the baryonic mass in the IGM contained within the telescope beam. We find similar baryonic mass surface densities for the three clusters and Coma: $\Sigma_G \sim 7 \times 10^{13}\ M_\odot\ \mathrm{Mpc}^{-2}$. For A2142, A2256, and Coma, consistent estimates of the baryonic mass fraction $M_{\mathrm{SZE}}/M_{\mathrm{tot}} \approx 0.061 \pm 0.010\ h^{-1}$. This is a lower limit on the total baryonic mass, as the galaxies contribute $M_{\mathrm{SZE}}/M_{\mathrm{tot}} \approx 0.009 \pm 0.003$. When compared with the standard primordial nucleosynthesis estimates for Ω_B, we find consistency between the SZE data and nucleosynthesis for cosmological density parameters in the range $\Omega_0 h \approx 0.21 \pm 0.05$. This agrees with the values determined independently from large-scale structure and galaxy counts. The cluster A478 gives a discrepant (high) fraction of $M_{\mathrm{SZE}}/M_{\mathrm{tot}} \sim 0.17\ h^{-1}$ and is likely elongated or heavily contaminated by the cooling flow (or both).

Recent determinations of Ω_B using the deuterium abundances in Lyman-α absorption systems along the line of sight to QSOs give discrepant values higher and lower than the standard. If we adopt a high baryon density $\Omega_B h^2 = 0.024 \pm 0.006$ (Tytler et al. 1996), then our data imply $\Omega_0 h \leq 0.39 \pm 0.12$. On the other hand, if $\Omega_B h^2 = 0.0062 \pm 0.0008$ (Rugers & Hogan 1996), then $\Omega_0 h \leq 0.10 \pm 0.02$.

By combining the measured SZE decrements with published X-ray models, we have determined the value of the Hubble constant implied for each of these clusters. Clusters A478 and A2142 are complicated by excess core emission attributed to cooling flows, and better X-ray models for the gas distribution must be obtained. A2256 appears to be undergoing a merging event, and additional modeling must also be done here. With the preliminary models gleaned from the literature, we obtain an average of $H_0 = 54^{+14}_{-13}$ km s^{-1} Mpc^{-1} for A478, A2142, A2256, and Coma. This average value tends toward the low side of the commonly accepted range, as do most of the other SZE determined values (see, e.g., Birkinshaw et al. 1991; Jones et al. 1993; Birkinshaw & Hughes 1994), though the large error bars place our measurement within 3 σ of practically all of the other values for H_0.

Note that the high baryon density of Tytler et al. (1996), our measurement of the baryon fraction, and our average value for the Hubble constant, would imply a high overall density for the universe $\Omega_0 \leq 0.72 \pm 0.29$. This is marginally consistent with a universe with the critical density $\Omega_0 = 1$. However, adoption of the lower values of the baryon density would favor the acceptance of a low density parameter.

Possible problems with using the SZE and X-ray measurements for inferring H_0 include substructure in cluster atmospheres, elongation of clusters along the line of sight, and the presence of cooling cores. The SZE decrement is sensitive to the outer regions of the intracluster gas, which have not been well studied because of their relatively faint X-ray emission. Better models of the cluster atmospheres will soon be provided by the new generation of X-ray satellites, such as *ASCA* and *AXAF*.

The advantage of determining H_0 from a well-selected sample of clusters is the ability to use the distribution of derived H_0 to test for variations in the astrophysical parameters of the cluster models assumed in the analysis. As this stage, our models are too uncertain, and therefore our error bars too large, to assess any but the grossest deviations in derived $h^{1/2}$. The most discrepant value is $H_0 = 32^{+18}_{-14}$ km s^{-1} Mpc^{-1} for A478, and even this is less than 2 σ from the mean. If massive clusters are inordinately elongated, estimates of H_0 from individual clusters may be off by a factor of 2 or more. Exclusion of A478 from the sample average raises the value of H_0 somewhat, though this step is unwarranted by the data at hand.

The ability to recognize deviant clusters like A478 demonstrates the power of using this sample of clusters. Clearly, completing the entire sample is the proper way to proceed using this method. However, the clusters reported here were selected as the first targets because they were free from strong contamination by radio sources. It will be very difficult to measure the SZE in the remaining clusters with the accuracy that we have been able to achieve with these first results.

In the end, it will be the distribution of the H_0 values for the sample that will tell us whether clusters are suitable tools with which to measure the expansion of universe or whether variations in shape and orientation, or density and temperature substructure, introduce severe limitations in the determination of H_0 by this method. Individual clusters are insufficient to make the case for one value of H_0 or another, and it remains to be demonstrated that this method will yield reliable results. In any event, sounding of the intragalactic medium through combined SZE and X-ray measurements promises to provide important constraints upon multiphase structures in the hot cluster atmosphere. This is as important as determining H_0, in that a number of cosmological tests, such as the baryon fraction Ω_B, rely upon observations of clusters of galaxies.

S. T. M. was supported by a R. A. Millikan Fellowship at Caltech. Experimental Microwave Astrophysics at Caltech is supported by NSF grant AST 91-17100 and AST 94-19279. S. T. M. also acknowledges the hospitality of the ITP in Santa Barbara, which is supported by the NSF under grant PHY 89-04035. The observations at the Owens Valley Radio Observatory could not have been made without the expert help of Harry Hardebeck, Mark Hodges, and Russ Keeney. We also thank Tim Pearson for creating the control software for the OVRO 5.5 m and 40 m telescopes and for many useful discussions.

REFERENCES

Abell, G., et al. 1989, ApJS, 70, 1
Abramopoulos, F., & Ku, W. H.-M. 1983, ApJ, 271, 446
Allen, S. W., et al. 1993, MNRAS, 262, 901
Andernach, H., et al. 1986, A&A, 65, 561
Baars, J. W. M., Genzel, R., Pauliny-Toth, I. I. K., & Witzel, A. 1977, A&A, 61, 99
Birkinshaw, M. 1990, in The Cosmic Microwave Background: 25 Years Later, ed. N. Mandolesi & N. Vittorio (Dordrecht: Kluwer), 77
Birkinshaw, M., & Gull, S. F. 1984, MNRAS, 206, 359
Birkinshaw, M., Gull, S. F., & Northover, K. J. E. 1981, MNRAS, 197, 571
Birkinshaw, M., & Hughes, J. P. 1994, ApJ, 420, 83
Birkinshaw, M., Hughes, J. P., & Arnaud, K. A. 1991, ApJ, 379, 466
Bond, J. R., et al. 1994, Phys. Rev. Lett., 72, 13
Brandt, N. 1992, B.S. thesis, Caltech
Bridle, A., et al. 1979, A&A, 80, 201
Briel, U. G., et al. 1991, A&A, 246, L10
Briel, U. G., Henry, J. P., & Böhringer, H. 1992, A&A, 259, L31
Carlstrom, J. E., Joy, M., & Grego, L. 1996, ApJ, 456, L75
Cavaliere, A., & Fusco-Femiano, R. 1976, A&A, 49, 137
Chase, S. T., Joseph, R. D., Robertson, N. A., & Ade, P. A. B. 1987, MNRAS, 225, 171
David, L. P., et al. 1993, ApJ, 412, 479
Davis, D. S., & Mushotzky, R. F. 1993, AJ, 105, 409
Edge, A. C., et al. 1990, MNRAS, 245, 559
Edge, A. C., & Stewart, G. C. 1991, MNRAS, 252, 414
Edge, A. C., Stewart, G. C., & Fabian, A. C. 1992, MNRAS, 258, 177
Efstathiou, G., Bond, J. R., & White, S. D. M. 1992, MNRAS, 258, 1P
Efstathiou, G., Sutherland, W. J., & Maddox, S. J. 1990, Nature, 348, 705
Fabian, A. C., et al. 1994, ApJ, 436, L63
Grainge, K., et al. 1994, MNRAS, 265, L57
Gregory, P. C. & Condon, J. J. 1991, ApJS, 77, 1011
Griffith, M. R., & Wright, A. E. 1993, AJ, 105, 1666
Henry, J. P., Briel, U. G., & Nulsen, P. E. J. 1993, A&A, 271, 413
Herbig, T. 1993, Ph.D. thesis, Caltech
Herbig, T., Lawrence, C. R., Readhead, A. C. S., & Gulkis, S. 1995, ApJ, 449, L5
Hughes, J. P., Gorenstein, P., & Fabricant, D. 1988, ApJ, 329, 82
Inagaki, Y., Suginohara, T., & Suto, Y. 1995, PASJ, 47, 411
Johnstone, R. M., et al. 1992, MNRAS, 255, 431
Jones, C., & Forman, W. 1984, ApJ, 276, 38
Jones, M., et al. 1993, Nature, 365, 320
Kennicutt, R. C., Freedman, W. L., & Mould, J. R. 1995, AJ, 110, 1476
Lake, G., & Partridge, R. B. 1980, ApJ, 237, 378
Mather, J. C., et al. 1994, ApJ, 420, 439
McMillan, S. L. W., et al. 1988, ApJ, 70, 723
Miyaji, T., et al. 1993, ApJ, 419, 66
Mould, J. R., et. al. 1995, ApJ, 449, 413
Myers, S. T., Readhead, A. C. S., & Lawrence, C. R. 1993, ApJ, 405, 8
Peacock, J. A., & Dodds, S. J. 1994, MNRAS, 267, 1020
Readhead, A. C. S., et al. 1989, ApJ, 346, 566
Rephaeli, Y. 1995, ApJ, 445, 33
Rugers, M., & Hogan, C. J. 1996, ApJ, 459, L1
Sandage, A. 1996, AJ, 111, 1
Smith, M. K., Kawano, L. H., & Malaney, R. A. 1993, ApJS, 85, 219
Sunyaev, R. A., & Zeldovich, Ya. B. 1980, ARA&A, 18, 537
Tully, R. B. 1988, Nature, 334, 209
Tytler, D., Fan, X. M., & Burles, S. 1996, Nature, submitted
White, S. D. M., & Fabian, A. C. 1995, MNRAS, 273, 72
White, S. D. M., Navarro, J. F., Evrard, A. E., & Frenk, C. S. 1993, Nature, 366, 429
Wilbanks, J., et al. 1994, ApJ, 427, L75
Wrixson, G. T., Welch, W. J. & Thornton, D. D. 1971, ApJ, 169, 171